Examination of Wheat Kernels for the Presence of Fusarium Damage and Mycotoxins using Near-Infrared Hyperspectral Imaging

By
Jennifer Brown

A thesis submitted to
the Faculty of Engineering
in partial fulfillment of
the requirements for the degree of
Master of Science

Department of Biosystems Engineering
University of Manitoba
Winnipeg, Manitoba

December 2014

Abstract

The agriculture industry experiences severe economic losses each year when wheat crops become infected with Fusarium and its associated mycotoxin Deoxynivalenol (DON). At the moment, the Canadian agriculture industry uses detection methods that are slow and labor intensive. This research investigated the feasibility of using near infrared hyperspectral imaging to detect Fusarium damage and its toxic by-product DON in Canadian Western Red Spring (CWRS) wheat. Four samples were selected from each grain grade resulting in a total of 16 samples and 240 hyperspectral data cube images were acquired by imaging kernels piled 1-2 layers thick. The data cubes were calibrated to the system and organized into 15 groups of 16 cubes. Consistent spectra from the groups were found and used to generate a 1- nearest neighbour classifier that could be used to find the percentages of spectra classified as each grade for all 240 data cubes. The percentages were used to generate two 3-nearest neighbour classifiers, one for identifying Fusarium damage and the other for identifying DON in a sample. The Fusarium damage classifier had an accuracy of 85%, a specificity of 65% and a sensitivity of 92%, while the DON content classifier had an accuracy of 80%, a specificity of 83% and a sensitivity of 77%. While a single sample image classification will not replace manual testing, the use of multiple samples from one harvest could reduce manual inspections.

Acknowledgements

I would like to thank my two thesis advisers Dr. Jitendra Paliwal and Dr. Jason Morrison, for helping me succeed at completing my Master of Science Degree in Biosystems Engineering. Their constant support and guidance throughout this process was greatly appreciated and helped me in all my endeavors for this thesis. In addition, thank you to Dr. Dilantha Fernando and Mr. Mark Hewko for providing me with advice and suggesting improvements for my thesis.

I would also like to thank Chella Vellaichamy and Ravikanth Lankapalli for teaching me how to operate the NIR HSI system and the multivolume pycnometer, as well as answering all my concerns and questions. As well, thank you to Chami Amarasinghe for providing me with photos for my thesis. I would like to thank Brenda Carter at Cargill Ltd. for providing funding and wheat samples for my thesis. In addition, thank you to Agricultural and Rural Development Industries for providing funding. I am thankful to Dale Bourns and Robert Lavallee for helping me build the locating jig that I required to perform my tests.

Finally, I would like to thank my friends and family for supporting and encouraging me throughout this process. I could not have done this without you.

Table of Contents

List of Tables

List of Figures

1 Introduction

This research investigated the feasibility of using near infrared (NIR) spectroscopy to detect a fungal infestation and its toxic by-product in wheat. As a key crop in Canadian agriculture the current reliance on human visual assessment and protracted destructive testing is a weakness in a multi-billion dollar industry. The feasibility of measurements for automatic quality classification of wheat is a possibility to augment or possibly replace the most fallible portion of the assessment process.

1.1 Motivation

In the world, Canada is a major producer and exporter of grain. In the 2011-12 crop year, Canada produced over 96.1 million tonnes of grain and exported 32 million tonnes of grain and wheat flour to other countries (Canadian Grain Commission, 2012; Statistics Canada, 2013). Current grains produced in Canada include wheat, oats, barley, rye, flaxseed, canola, soybeans, peas and corn. Wheat is the most abundantly grown grain across Canada (i.e. 27.2 million tonnes in 2011) and is the most exported (i.e. 13.3 million tonnes in 2011). Upon harvesting, crops are either stored in silos or transported to local elevators. At the elevators crops are received, inspected for grade (i.e. quality), weight, protein, moisture content and dockage, and stored. When grain is sold, it is transported by railcars to a main elevator and exported across the world.

Increased competition in today's markets is the driving force behind Canada's exportation of top quality grain (Agriculture and Agri-Food Canada, 2013). This reputation is maintainable only if large quantities of grain are produced at consistent

qualities. A higher quality of the harvested grain equates to a higher grade during inspection and to higher revenue for producers. The Canadian Grain Commission has implemented strict guidelines and regulations to maintain a high standard for grain (Justice Laws, 2013). At the moment, grain is assessed based on a visual method. An inspector examines a representative sample of the grain for weight, kernel vitreousness, protein and degree of soundness (i.e. does the grain exhibit damage due to frost, insects or fungi). The grain is then graded based on these criteria and that determines the potential revenue/profit. This grading system is subject to error, is slow and can result in misclassification of grain (Dowell et al. 1999). To correct these problems, research has focused on discovering techniques that are fast, portable, reliable and consistent for grain quality evaluation.

1.2 The Problems Faced In Industry

Grain is susceptible to numerous threats while in the field and afterwards in storage. It is vulnerable to damage inflicted by the weather (i.e. extreme heat or cold, draught and excess moisture), pest and fungal development infestations. Focusing on potential fungal threats, wheat kernels are examined for the presence of a particular fungal species in the genus *Fusarium*. This genus of fungus consists of different species including: *F. culmorum*, *F. graminearum* and *F. avenaceum.* Of these species *F. graminearum* is of interest because it is most prevalent in North America. It causes permanent damage to kernels through an infection known as Fusarium head blight (FHB), which creates a significant decrease in crop yields by affecting up to 50% of kernels and lowers the grain's grade (Dowell et al. 1999). The kernels undergo a reduction in weight and an alteration in the colour from golden to white bleached. In addition, kernel damage lowers

the quality of flour colour, ash content and baking performance of wheat products (Shahin & Symons, 2011). The constant occurrence of FHB creates the requirement for inspection and separation of sound kernels from damaged kernels in grain crops. The risk of consuming FHB infected kernels decreases by limiting the amount of damaged kernels allowed in crops. The current method of grain inspection relies on manual assessment of each kernel from a sample group and checks for signs of damage. The entire yield is downgraded when the percentage of damaged kernels exceeds a predetermined threshold (Delwiche, 2003). Another concern is that kernel inspection is subject to the inspectors' judgments, which are influenced by experience, fatigue and their work environment. These factors can cause the inspector to miss crucial characteristics of kernels resulting in misclassification (Dowell et al. 1999). Furthermore, manual inspection can miss early stages of infection when there is no visual damage to the kernels (Shahin & Symons, 2011; Clear and Patrick, 2010). For these reasons, the current technique of kernel observation by inspectors is slow, time consuming and prone to error. An ideal replacement is an accurate and objective assessment technique that can be implemented at various levels of grain handling.

A further issue with Fusarium infected wheat kernels is an increased risk of mycotoxin development. Mycotoxins are secondary metabolites produced by fungi and some well known examples are aflatoxins, citrinin, ergot alkaloids, fumonisins, patulin, zearalenone and trichothecenes (Bennett & Klich, 2003). Trichothecenes, such as deoxynivalenol (DON), are associated with Fusarium in wheat kernels and are toxic upon consumption. Kernels with higher Fusarium damage increase the occurrence of DON content, but it is difficult to correlate because DON content can occur with lower

Fusarium damage as well (Dowell et al. 1999). The problem with mycotoxins, like DON, is it causes harmful effects in animals and humans. The desire to avoid the occurrence of nausea, vomiting, diarrhea and reproductive abnormalities creates a demand to detect DON and prevent the infected kernels from being processed and consumed.

1.3 Research Objectives

The focus of this thesis is to determine the validity of applying near infrared hyperspectral imaging (NIR HSI) as a detection method for Fusarium damage and DON content. As a whole, NIR HSI possesses the required qualities to be successful and has numerous applications in similar areas of research. The specific objective for this research was to create two classifiers that utilize NIR HSI: one for determining the presence of Fusarium damage and the other for determining the presence of DON content in a given sample.

The remainder of this thesis includes the literature review, materials and methods, results and discussion, conclusion and recommendations. The literature review describes the background and theory on NIR HSI, instrumentation, calibration techniques and the information on Fusarium, The materials and methods section outlines the NIR HSI system specifications & system setup, camera temperature distribution, the reflectance standards and the procedures for calibration, outlier determination, data acquisition and data analysis. The results and discussion section provides the results and explains how the results are meaningful. The conclusion section summarizes the research that was accomplished through this thesis and concludes on the results found. Finally, the recommendation section suggests potential areas that require future work.

2 Literature Review

2.1 Background on Near-Infrared Hyperspectral Imaging

NIR HSI is a combination of spectroscopy that uses the NIR portion of the electromagnetic spectrum and hyperspectral imaging which collects a spectrum at each pixel of an image. The electromagnetic spectrum is composed of a wide range of electromagnetic radiation at various wavelengths creating an overlap of regions (Gonzalez & Woods, 2008). On one extreme of the spectrum is gamma ray radiation, which has the shortest wavelengths (e.g.>10 pm) and the highest energy levels. Following gamma rays is x-rays (e.g. 10 pm to 10 nm), ultraviolet radiation (e.g. 10 nm to 400 nm), visible radiation (e.g. 400 nm to 750 nm), infrared radiation (e.g. 750 nm to 1 mm), microwave radiation (e.g. 1 mm to 10 cm), and then finally radiofrequency radiation (e.g. 10 cm to 10 km) (Mortimer, 1993). Infrared radiation is the radiation of interest for this research and it is subdivided into near-infrared (e.g. 750 nm to 2500 nm), mid-infrared (e.g. 2500 nm to 5000 nm), and far-infrared (e.g. 5000 nm to 1 mm) (Bosco, 2009). In summary, the spectrum increases in wavelength from gamma radiation to radiofrequency radiation while decreasing in frequency and energy (**Figure 2.0**).

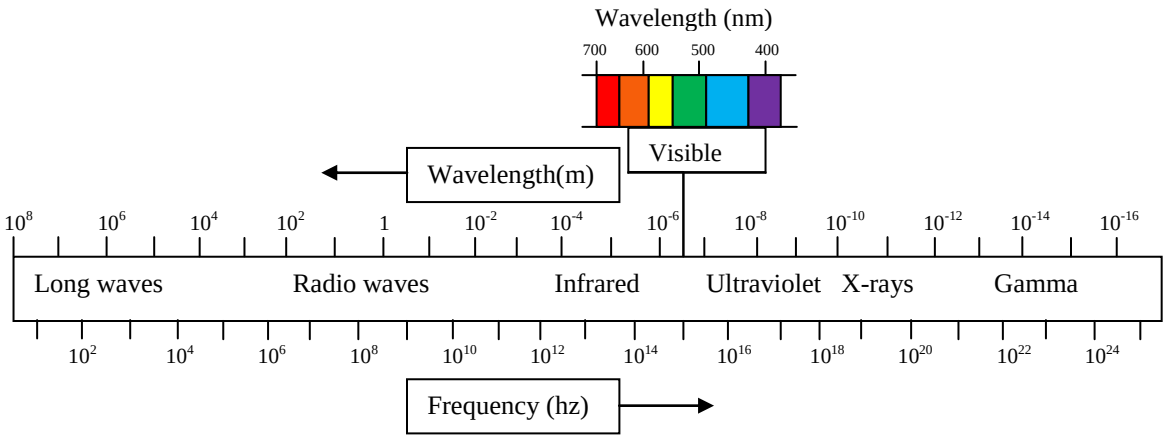

Figure 2.0 Electromagnetic Spectrum. *Source:* Vandergriff, 2013.

The NIR region was first discovered in 1800 by the astronomer Sir William Herschel when examining the development of heat on a telescope (Bosco, 2009). The next substantial contribution occurred 100 years later with the collection of spectra compounds using NIR spectroscopy by W.W. Coblenz. In 1940, Sir Thomas Ralph Merton developed a "way of ruling diffraction grating of high optical quality", which led to the collection of high resolution spectra. Ten years later, William Kaye described the aspects of NIR, such as the spectra, the applications and the instrumentation. In the 1960's, new interest in NIR developed with Karl H. Norris predicting the moisture content of wheat flour using NIR wavelengths (Bosco, 2009). In the 1970's, Phil Williams suggested that NIR spectroscopy could be applied to inspecting protein in wheat kernels when unloaded from rail cars. Williams realized that NIR spectroscopy was a fast technique that replaces the slow chemical tests and brought this knowledge to the attention of the Grain Research Laboratory. By the late 1970's NIR spectroscopy was accepted as an international standard procedure and used by major grain companies to verify grain quality. Finally, with the development of NIR whole grain analyzers, NIR spectroscopy was brought into focus and gained world-wide acceptance.

NIR spectroscopy has many qualities that make it an excellent technique, but NIR has a drawback (Wang & Paliwal, 2007). NIR spectroscopy collects spectra that are one dimensional, which means the spectral distribution of chemical compounds is lost. A solution to this problem is to combine near-infrared spectroscopy with the hyperspectral imaging technique. Hyperspectral imaging creates a three dimensional data cube of information, allowing no loss of spectra. Between 1960 and 1990, the applications for spectral imaging consisted of "astrophysics, remote sensing and terrestrial military" (Fischer & Kakoulli, 2006). Multispectral imaging was the first name given to the technique, but with the development of hardware to collect continuous or large number of spectral bands, it was renamed hyperspectral imaging. Within the past 20 years, semi-conductors and focal plane arrays have added to the development of this technology. Hyperspectral imaging has spread into other fields, such as medicine, pharmacology, environmental sciences, food engineering, agriculture and the management of natural resources (Fischer & Kakoulli, 2006).

2.2 Near-Infrared Hyperspectral Imaging Theory

Spectroscopy is the study of how electromagnetic radiation interacts with matter through absorbance and reflectance (Mortimer, 1993). Reflectance is the resulting radiation that either travels through a sample and is reflected back through the sample or contacts the surface of a sample and behaves as a mirror reflecting the radiation. It is represented by:

$$R = \frac{P}{P_0} = \frac{I}{I_0} \tag{2.1}$$

where P is the radiant power (i.e. the radiation measured coming from the sample) and P_0 is the incident power (i.e. the radiation first coming in contact with the sample) (Banwell

& McCash, 1994; Osborne et al., 1993). Reflectance can also be represented in terms of intensity, where I is the radiation intensity exiting the sample and I_0 is the radiation intensity entering the sample (Banwell & McCash, 1994). Reflectance occurs when radiation contacts the surface of a sample and behaves as a mirror reflecting the radiation. This behavior follows the law of reflection that states the incident ray, the reflected ray and the line perpendicular to the mirror surface all occur in the same plane (i.e. the plane of incidence). Furthermore, the law states that the reflected ray angle will be equal to the incident ray angle. The type of sample determines how the radiation reacts with the sample. The radiation can either experience spectral reflectance (i.e. the light experiences reflection) or diffuse reflectance (i.e. the light experiences a combination of reflectance, refraction and scatter due to complex interfaces at and inside the sample) (Osborne et al., 1993).

Absorbance is achieved by shining a beam of radiation onto a sample causing the atoms to absorb the photon energy. The atoms translate the infrared energy into kinetic energy becoming excited and moving from the ground energy state to higher energy levels. When the atoms drop back down to the ground energy state, photon energy is released and this is called spontaneous emission. A stimulus of radiation is required if the atoms do not release the energy, which results in a stimulated emission and an amplification of radiation (Pedrotti, 2013). Absorbance can be denoted as:

$$A = \log\left(\frac{P_0}{\mathrm{P}}\right) = \log\left(\frac{\mathrm{I}_0}{\mathrm{I}}\right) = \log\left(\frac{1}{R}\right) \qquad (2.2)$$

where absorbance can be represented in terms of power and radiation intensity (Osborne et al., 1993).

Hyperspectral imaging works by creating a data cube or “hypercube” of spectral information. When the NIR equipment operates, the amount of reflection from the sample at each wavelength is recorded and stored as one slice. The slices continue to accumulate until all the reflections at each wavelength are accounted for and results in a cube of data. The data cube consists of two spatial dimensions $i \times j$ that represents each pixel of the image and one spectral dimension k that represents the wavelengths. The hypercube can be queried and observed in multiple ways to extract information on the chemistry of the sample (Feng & Sun, 2012).

2.3 Instrumentation

The instrumentation involved with the NIR HSI system used in this research has four main components: the illumination source, the filters, the optics and the detector. The system operates by shining the illumination source onto a sample, causing the sample to absorb and reflect the radiation. The radiation reflected by the sample is directed towards the filters above the sample. The filter allows a particular band of wavelengths through for a specific exposure time and that radiation passes to the lens of the camera. The lens converges the radiation towards the photodetector, which detects and records the amount of radiation coming in contact with it.

The purpose of the illumination source is to provide the electromagnetic radiation in the desired range to the sample. The illumination source acts as an excitation source and causes the molecules in the sample to vibrate enough for the photodetector to detect the energy. Without the illumination source the subject would produce weak radiation, which is not practical for measurement. Illumination sources are generally divided up into two categories: thermal sources and non-thermal sources. Thermal sources are

incandescent bulbs that produce broadband energy covering the visible and entire NIR region, which is ideal for instruments operating in the NIR range. The majority of NIR instruments utilize tungsten filament bulbs as a thermal illumination source because of the bulbs' long lifetime. Quartz halogen bulbs are an alternative option to the tungsten filament bulbs and allow the bulbs to reach higher temperatures, but are brittle and can become vulnerable to mechanical shock. Non-thermal sources produce narrow bands of energy and examples are discharge lamps, light-emitting diodes, laser diodes and lasers. The main advantage of non-thermal sources is their higher efficiency when compared to thermal sources (Osborne et al., 1993).

The filter's purpose is to narrow the broad bands of radiation down to a specific wavelength in the NIR HSI system. By narrowing and isolating the radiation, the filters allow the system to record the sample's reaction to the NIR radiation localized to a wavelength. Multiple types of filters can be chosen when designing a system, including fixed filters, wedge filters, prisms and tunable filters (Ozaki et al., 2007). Tunable filters are generally of two types: acousto-optical tunable filters (AOTF) and liquid crystal tunable filters (LCTF). AOTFs have a high efficiency and separate wavelengths quickly without any moving parts. LCTFs are a stack of polarized plates that determine the speed of transition between wavelengths based on the relaxation time of the plates (Ozaki et al., 2007). While the mechanisms of operation for AOTF and LCTF are different, the end result is similar with the radiation separated for contact with the lens.

The lens operates by either converging or diverging the incoming radiation based on the material it is made of and its shape. The type of material composing the lens can affect how the waves of radiation interact because different materials have different

refractive indexes. Lenses come in multiple different shapes like, biconvex, plano-convex, plano-concave and biconcave. The shape of a lens determines if the lens is considered a positive lens (i.e. converging) or a negative lens (i.e. diverging). If the lens is positive it focuses the wavelengths towards a focal point and if the lens is negative it directs the wavelengths outwards (Pedrotti, 2013**)**.

The photodetector detects the reflected radiation that comes into contact with it, converts it into an electrical signal and stores the information into an array. Photodetectors are composed of individual sensors that vary in material because of the wide ranges of wavelengths detected. Silicon based materials called charge coupled devices (CCDs), detect in the 700-1000 nm range and are known for their high efficiency (Osborne et al., 1993). CCDs are semiconductors composed of a *p*-*n* junction that has a bandgap separating the conduction band from the valence band. Upon contact with the semiconductor, the radiation is absorbed causing the excitation of an electron to jump from the valence band to the conduction band. When the electron falls back down to the valence band the radiation is emitted and recorded (Osborne et al., 1993). Another sensor material is indium gallium arsenide (InGaAs), which detects in the optimal range of 1000-1800 nm for NIR radiation.

2.4 Calibration

Calibration of the NIR HSI equipment is instrumental in collecting accurate and reliable data. Thorough research in the area of NIR HSI calibration resulted in finding two papers on the topic. Geladi et al. (2004) and Burger & Geladi (2005) reported a calibration technique for a hyperspectral imaging machine operating in the NIR spectral range using liquid crystal tunable filters combined with an InGaAs photodetector. Their

recommendation is to calibrate with certified Spectralon tile standards from Labsphere because the standards have known reflectance values. The standards reflect the desired amount of radiation towards the photodetector that are recorded as A/D counts. These reflected values are used to determine the calibration coefficients for each pixel at each frequency. There are three calibration models to choose from: one-point, linear and quadratic calibration. A one-point calibration equation is:

$$X = 100(S - B)(W - B)^{-1} \quad (2.3)$$

where X is the hyperspectral image in percent reflectance, S is the sample data cube, B is the dark current image and W is the 100% reference image (i.e. the 99% standard is used because it is closest to 100%). A linear calibration equation is:

$$y_{ijk} = \propto_{ijk} + \beta_{ijk} r_{ijk} + \varepsilon_{ijk} \quad (2.4)$$

where y_{ijk} is the calibrated reflectance vector, β_{ijk} is the slope, $\propto_{ijk}$ is the constant, r_{ijk} is the dark current corrected measured reflectance signal, and ε_{ijk} is the residuals. A similar quadratic calibration equation is represented by:

$$y_{ijk} = \propto_{ijk} + \beta_{ijk} r_{ijk} + \gamma_{ijk} {r_{ijk}}^2 + \varepsilon_{ijk} \quad (2.5)$$

where γ_{ijk} is the quadratic coefficient.

Geladi et al. (2004) and Burger & Geladi (2005) both recommended blurring (i.e., de-focusing) the image before data acquisition of the reflectance standards to remove the risk of the camera picking up the textures, local imperfections, on each standard's surface. By blurring the image it allowed for homogenous images. Also, through testing it was seen that quadratic calibration models performed the best over one point and linear

calibration. For better results with the quadratic calibration equation, more than four reflectance standards should be selected.

2.5 Near-Infrared Hyperspectral Imaging as a Detection Method for Fusarium

2.5.1 Background on Fusarium

The fungal disease FHB causes dramatic changes to the kernels of wheat, barley, rye and maize (Goswami & Corby Kistler, 2004). FHB is caused by species belonging to the *Fusarium* genus, which consists of numerous species across the world. From the entire genus, the species of interest are *F. culmorum*, *F. graminearum* and *F. avenaceum* because of their direct involvement with infecting grain (Booth, 1971). In North America, *F. graminearum* is the most prevalent cause of FHB. During the winter months the fungus lays dormant in the crop debris until spring when the weather becomes warm and moist. The fungal structure matures with the crop and releases ascospores by means of rain, wind or insects when the grain begins to flower (**Figure 2.1**).

Figure 2.1 An infected field of wheat

In the case of wheat, the spores come in contact with the plant spikes and either penetrate the epidermis or extend around the outside. The fungus spreads from floret to floret inside a spikelet and then from spikelet to spikelet until it takes over the kernels (Goswami & Corby Kistler, 2004). The infected kernels are known as scab or tombstone because of the altered appearance of the kernels. The characteristics of FHB vary due to infection intensity, but the standard appearance is shrunken shriveled kernels with a reduction in weight and a colour change to bleached white/pink (Delwich, Kim, & Dong, 2011) (**Figure 2.2**).

Figure 2.2 Fusarium infected wheat kernels

The kernels are considered undesirable because processed infected kernels have negative effects on flour colour, ash content and baking performance (Dexter et al., 1996). As the FHB causes physical changes to the kernels it also causes a reduction in crop yields.

The infection of FHB on grain causes a severe economic impact on the agriculture industry with up to $3 billion in losses to American farmers and $200 million in losses to Canadian farmers of wheat and barley since the 1990s (Windels, 2000). The more infected the grain crop becomes, the greater the economic losses to the farmer because less viable grain is being produced. This causes a hardship on the industry when FHB

spreads across the North American plains and creates an epidemic. From 1993 to 1999, FHB epidemics occurred and increased in intensity each year. Furthermore, FHB has spread across North Dakota into South Dakota and Minnesota and from southern Manitoba into Saskatchewan. The trend of FHB spreading across North America has motivated funding towards bringing awareness to increasing tillage of fields, alternating planted crops and spraying fungicides at peak times for disease (Windels, 2000). The goal is to hinder the opportunities for fungus growth and reduce the risk of another epidemic outbreak.

In Canada there are two wheat classes based on harvest location, eastern and western. The eastern Canadian wheat is subdivided into seven subclasses, while the western Canadian wheat is subdivided into eight subclasses. Each subclass is specific to a type of wheat and holds true to specific characteristics (Canadian Grain Commission, 2012). A wheat class of interest in this research is Canadian Western Red Spring (CWRS) and is characterized by being translucent red in colour, small to midsize in size, oval to ovate in shape and possesses a round, midsize to large germ (Canadian Grain Commission, 2012). Also, the CWRS wheat has superior milling and baking qualities and is for making multiple types of bread and pasta (Canadian Grain Commission, 2008). When a crop is harvested it is placed into storage on farms until it is ready for sale and loaded into railcars to be transported to stations, where representative samples are taken for grading and testing (Bosco, 2009). Grading procedures have been implemented by the Canadian Grain Commission (CGC) in order to reduce the amount of damaged kernels unexpectedly entering production lines (Shahin & Symons, 2011). Each type of grain is divided into grades and for CWRS there are five grades: No. 1 CWRS, 2 CWRS, 3

CWRS, 4 CWRS and CW feed. The best grade is No.1 CWRS and under the guidelines, as seen in **Appendix C**, the grade decreases to the lowest grade CW feed. Visual examinations are performed by inspectors using a 10* magnifying glass to determine Fusarium damage on sample kernels (Shahin & Symons, 2011). This process is time consuming because low levels of Fusarium damage on the kernels do not express the known characteristics. Inspection times are improved for higher infection levels because the kernels exhibit the FHB characteristics. Another method for detecting Fusarium damaged kernels is to run the samples through a gravity table, which separates the kernels based on density. This method operates by combining air flow, deck incline and the oscillation frequency together to separate the kernels (Tkachuk et al., 1991; Dexter et al., 1996).

In addition to causing permanent changes to kernels and economic losses to farmers, FHB has been linked to mycotoxins. This secondary metabolite of fungi has toxic effects on humans and animals upon consumption (Peraica et al., 1999). The intensity and kind of symptoms developed depend on the type of mycotoxin being produced. The major mycotoxins are aflatoxins, citrinin, ergot alkaloids, fumonisins, patulin, zearalenone and trichothecenes (Bennett & Klich, 2003). In addition, each fungus produces certain mycotoxins and each mycotoxin can be produced by different fungi. This makes the identification of the fungus more difficult. Of these seven toxins, fumonisins, zearalenone and trichothecenes are produced by Fusarium (Krska et al., 2007). Fumonisin has been detected in corn and can cause severe problems in animals and is linked to esophageal cancer in humans. Zearalenone is found in wheat, sorghum, barley and maze, and causes infertility and reproductive problems in animals. Finally

there are trichothecenes, which are the mycotoxin of interest because DON belongs to this mycotoxin family and is the primary mycotoxin produced by *F. graminearum* (Bennett & Klich, 2003).

Trichothecenes are found in mold-infected grains (i.e. wheat, oats, barley and rye) and cause less lethal symptoms when consumed than other mycotoxins (Bennett & Klich, 2003; Childress et al., 1990; Peraica et al., 1999). In the case of DON, the symptoms are typically less harmful than other trichothecenes, but still cause health hazards when ingested in large quantities (Bennett & Klich, 2003). In humans, DON causes symptoms of vomiting, headaches, dizziness, diarrhea and nausea (Pieters et al., 2002). In animals, DON consumption at low quantities causes food refusal and weight loss. The characteristic symptoms of DON ingestion has given rise to alternative names, such as vomitoxin and food refusal factor (Bennett & Klich, 2003). Overall, the combination of negative affects and ease of occurrence makes DON detection a priority. The methods of DON detection are different from Fusarium detection methods because DON is miniscule. DON detection methods involve chemical testing, like enzyme linked immunosorbent assay (ELISA), gas chromatography, high performance liquid chromatography, thin layer chromatography and mass spectrometry (Childress et al., 1990; Shahin & Symons, 2011). These methods are slow and tedious because samples are sent for testing. The agriculture industry wants a method that detects Fusarium damage and DON content with immediate results, in order to isolate and remove contaminated grain.

2.5.2 Suitability of Near-Infrared Hyperspectral Imaging

Currently simple, but tedious techniques exist for detecting Fusarium and DON infected kernels. These tests are accurate, but are not fast or portable. Since the approaches are also tedious, research, including this thesis, is underway to find faster solutions to the task. A variety of research has been performed to detect Fusarium damage and DON in kernels. Examples of techniques include hyperspectral imaging (Bauriegal et al., 2011), Fourier transform infrared microspectroscopy (Starr, 2011), PCR array (Parry & Nicholson, 1996), immunoassay (De Saeger & Van Peteghem, 1996) and mid-infrared spectroscopy (Kos et al., 2003). The techniques lack the ideal qualities (i.e. fast, portable, reliable and works well with biological samples) and resulted in limited successes for the detection of Fusarium damage and DON content in the kernels. The previously described difficulties have led to continued research exploring the use of NIR HSI as a novel detection procedure.

NIR HSI has multiple advantages that make it an excellent choice for detecting Fusarium damage and DON in grain. NIR HSI is fast, non-destructive to samples, yields great results with biological samples, is portable and inexpensive (Bosco, 2009; Wang & Paliwal, 2007). NIR HSI is fast because it produces spectra at a fast pace, requires no sample preparation before data acquisition and could be applied in the field (Blanco & Villarroya, 2002). NIR HSI is non-destructive to samples because the NIR radiation penetrates into the sample, resulting in no sample preparation (Blanco & Villarroya, 2002). Also, NIR HSI produces spectra from biological samples that provide chemical and physical information ideal for analyzing such samples. A variety of advancements in NIR HSI technology has led to portable instruments that can go to the field for multiple

applications and can even be mounted on a truck (Blanco & Villarroya, 2002; Bosco, G.L, 2009). Finally, NIR HSI is an inexpensive technique because it has almost no moving parts, resulting in fewer break downs less maintenance (Blanco & Villarroya, 2002). Overall, NIR HSI possesses all of the desired characteristics and has applications in many different fields making it a natural choice for detection of fungi and mycotoxins.

2.5.3 Near-Infrared Applications Related to Detection of Fusarium

NIR technology can be used in numerous fields, resulting in a wide range of applications. NIR is used in the agricultural industry by examining the composition of food, such as grain moisture content and protein quality, milk and dairy products, and fruits and vegetables (Blanco & Villarroya, 2002). Also, NIR can assess the quality of meat, fruit ripeness, handling defects, the level of caffeine in coffee, farm feed contamination and crop infections (Blanco & Villarroya, 2002; Bosco, 2009; Wang & Paliwal, 2007). Furthermore, NIR has applications in the pharmaceutical, environmental and petrochemical industries (Blanco & Villarroya, 2002). Focusing on the agricultural industry, researchers have experimented with different combinations of spectral ranges and analysis tools to optimize the quality of results. Samples for the experiments can be tested as individual kernels or in the field as entire ears of wheat. The goal is to find which wavelengths, analysis approaches, and sampling techniques work well together to detect Fusarium damage and then subsequently DON content. Successes in these experiments will lead to further development of faster, more effective techniques for detection.

One approach to detecting Fusarium damage and DON is to harvest the kernels. Dowell et al. (1999) collected 10 samples of hard red spring wheat kernels and selected

45 kernels from each sample. They performed NIR imaging in the range of 400-1700 nm and the data cubes were analyzed with partial least squares regression. Chemical testing was performed on each ground kernel to determine levels of ergosterol and DON. It was found that in kernels with Fusarium symptoms had levels of DON and ergosterol. Even kernels with no visible signs of Fusarium damage had small levels of DON and ergosterol. The researchers created a calibration equation with six factors and it was found that they correctly classified damaged kernels that were confirmed by visual inspection. Also, their calibration accounted for more kernels with DON content than observed. Dowell et al. (1999) noted that calibration is good at identifying kernels not visible with damage, but still high in DON. It was found that as the weight in kernels decrease, the levels of DON and ergosterol increases. This can occur either because smaller kernels have more DON and ergosterol inside or damaged kernels are less dense. Important wavelengths for O-H absorbance were 750, 950 and 1400 nm, C-H absorbance were 1200, 1400 and 1650 nm, and N-H absorbance were 1050 and 1500 nm. They concluded that NIR can detect Fusarium damage, DON and ergosterol in single kernels.

Polder et al. (2005) selected 96 wheat kernels that were artificially infected with *F. culmorum* and tested in the visible (430-900 nm) and NIR (900-1750 nm) spectral ranges. The researchers chose to examine the transmitted spectra instead of the reflected spectra since Fusarium is found on the inside and outside of the kernels. Masks were applied to the data cubes to obtain better images by taking into account the dark and saturated pixels. They used TaqMan, a real-time polymerase chain reaction (PCR) analysis, to detect Fusarium on individual ground kernels. Finally, data preprocessing and partial least squares were the supervised methods performed, while fuzzy c-means clustering

was the unsupervised method performed on the data cubes. The researchers discovered that the kernels with high levels of Fusarium absorb more light than kernels with lower levels. The partial least squares regression performed better on the NIR images than the visible images and the fuzzy *c*-means identified infected kernels with about 6000 pg of Fusarium. They concluded that higher levels of Fusarium are easier to detect than lower levels in kernels.

Shahin & Symons (2011) performed an experiment on 400 CWRS kernels in the visible to NIR spectral range (400-1000 nm). All the kernels were inspected and graded into two categories, good and Fusarium damaged kernels (FDK). The FDK were further classified as either mild or severely damaged. They employed a pushbroom hyperspectral imaging system and upon scanning created data cubes 800×400×218. The cubes contain images of kernels lined up in three rows of good, mild and severe. A mask was created to help remove the distraction of the background in the images and then principle component analysis (PCA) was applied to the cubes. Six wavelengths were selected based on the PCA results and PCA was run again on those wavelengths. Linear discriminant analysis was applied to the results to create classification models. These models distinguish between good and severe and then severe and mild kernels. They concluded that the spectral range of 400-1000 nm was able to detect levels of Fusarium damage in the kernels and distinguish between them.

Delwiche et al. (2011) selected eight wheat subsamples from larger sample sets and acquired images of the samples using NIR HSI. For each subsample, kernels were ranked from most infected to most healthy. Eight of the most infected were placed into a row and then eight of the healthiest were placed in a row below the infected kernels. Once the data

cubes were created masks were utilized to remove the effect of the background on the images. A t-test was performed to confirm that the pixels have different levels for healthy and damaged kernels and the pixels were averaged for each kernel. Also, they distinguished between the endosperm and germ of the kernels using the pixels. Models were created from the wavelengths using linear discriminant analysis and cross-validated with the high contrast models. Their conclusion was that, NIR was better at identifying damage over visible light using wavelengths 1200, 1420 and 1560 nm.

Overall, considerable time and effort has been put towards finding a detection and analysis method that is consistent and successful. Each study has yielded limited success in Fusarium detection and concluded that further research needed to be performed. This thesis continues the research and aims to detect Fusarium damage and DON content with an NIR HSI system.

3 Material and Methods

3.1 System Specifications and Setup

The NIR HSI system used to conduct this research was composed of four main components: the illumination source, the filters, the optics and the detector. The illumination source employed was two halogen incandescent bulbs located on either side of the camera (**Figure 3.0**). The bulbs (model No. M40189, Bencher Inc., Antioch, IL) had a power rating of 300 W. The filters involved were two automatic VariSpec (Perkin Elmer, Waltham, MA) LCTFs with an aperture of 20 mm and a full width at half maximum bandwidth of 10 nm. To cover the entire spectral range required one filter operates between 650-1100 nm and the other operates between 850-1800 nm. Following the filters was a silica glass lens with an antireflective coating made of MgF_2. The lens (model No. L25F0.95, Electrophysics Inc., Fairfield, NJ) had an aperture of F1.4 and a focal length of 25mm. The detector was an InGaAs FPA (Sensors Unlimited Inc., Princeton, NJ) that consisted of 640*477 detectors, where each detector was 27*27µm and operated in the 900-1700 nm spectral range. The camera had a power supply, a PCI data acquisition board with 12 bit resolution and was controlled by a desktop computer. The computer was a Dell Optiplex GX280 with a 3 GHz Intel Pentium 4 processor 1GB of RAM.

The camera, lens and filters were attached as a unit in a vertical position off of the main stand, where each were stacked facing downwards with the camera being the farthest from the platform and the filters being the closest. The problem with this set up was the filters had an aperture of 20 mm, while the camera had an aperture of 25 mm.

This means that the aperture of the filters limits what was detected by the camera because the filter comes into contact with the radiation off the sample first. The camera was attached to the main stand by an adjustable crank and that allows for changing the height between the unit and the platform. Also, at that same attachment there was the option of moving the unit forward or backwards over the platform and to tilt the unit. This was ideal because it allows for control over where the camera rests over the platform, as well as what is seen by the camera. For this thesis the LCTF was positioned 54.0 mm vertically over the platform, the backside of the LCTF was 174.6 mm away from the main stand and the tilt is set at 0º. In addition, the f-stop on the lens was set to the option 1.4, which was the maximum setting and had the largest aperture. The f-stop, also known as the focal ratio, f-number and relative aperture, was the ratio of the focal length to the aperture and controls the light passing towards the camera.

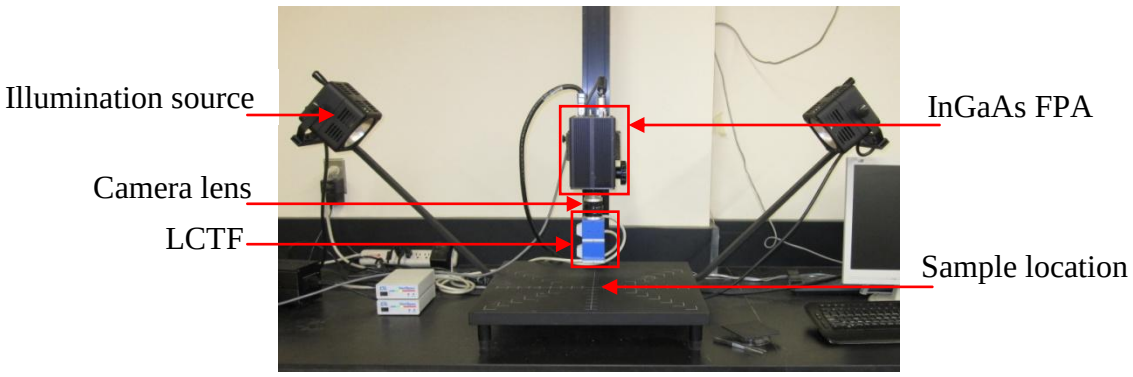

Figure 3.0 Near-Infrared Hyperspectral Imaging system configuration

Before operating the NIR HSI system, each component must be turned on and allowed to stabilize for 60 minutes. As the system warms up the computer was turned on and the program UofMInGaAs.vi was loaded (**Figure 3.1**).

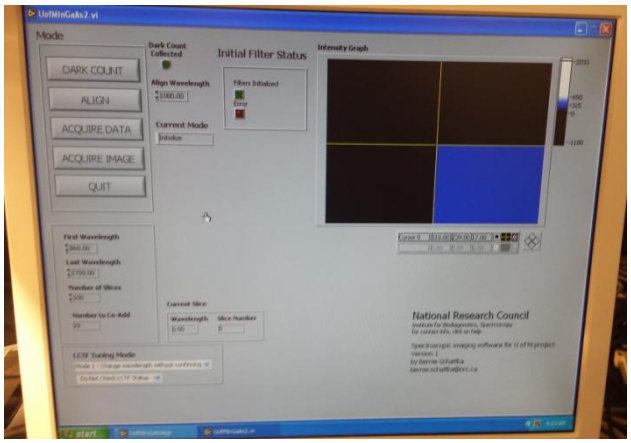

Figure 3.1 Screen shot of the UofMInGaAs computer program

There are options that can be adjusted to create the desired experiment conditions. The align wavelength was set to 1350 nm to ensure a central wavelength was focused, the first wavelength was set to 960 nm and the last wavelength was 1700 nm. The number of slices was the number of wavelengths to be examined and set to 100. Finally the number of co-additions was set as 10 to improve the signal-to-noise ratio (SNR) in areas where the detectors were less sensitive. Data acquisition began once the system warmed up and the filters initialized.

3.2 Camera Temperature Distribution

The halogen illumination bulbs produce the illumination source for the system, but they also lose a great deal of energy as heat. This additional heat warms up the LCTF, the lens and the camera. The temperature distribution and peak temperature were monitored to ensure the temperature does not exceed the 40°C operating temperature of the camera. If the temperature were to exceed the maximum temperature of the camera, it could interfere with the results or even damage the camera. Furthermore, the temperature was monitored to verify that the system was operating at a uniform temperature and there

were no irregularities that could influence results. The length of time for the system to reach a constant temperature was measured and provides the required warm up time before data acquisition. Two k-type thermocouples were hooked up to a 34972A LXI data acquisition system from Agilent to monitor the temperature change. The results were recorded and displayed using the BenchLink data logger software on a laptop computer. Each thermocouple was taped flush against the camera of the NIR system, where one thermocouple was placed on the right side of the camera and the second thermocouple was placed on the left side and the temperature change was recorded from initial system turn on until the temperature plateaus. To simulate working conditions the NIR system scanned a 99% reflectance standard while the data logger recorded the increasing temperature. After the scan was complete the data logger was stopped for an interval of five minutes and then started again for a new scan. This process repeated until there was no notable change in the temperature. Upon reaching a plateau the NIR system components were turned off and then monitored in five-minute intervals for the length of time required to reach room temperature again. Once the NIR system cooled down the thermocouples were moved to a new position on the camera and a new temperature acquisition began. The three thermocouple locations can be seen in **Figure 3.2**.

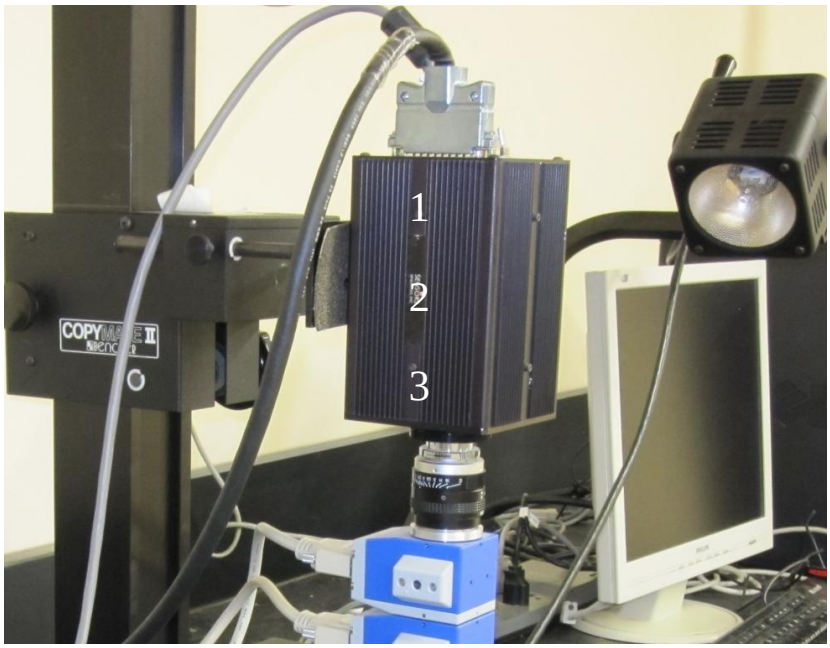

Figure 3.2 Thermocouple locations on the camera

Also, the light source had two intensity options of high and low, both were monitored to determine the temperature difference. The system was allowed to heat up and cool down twice on the low setting. Finally, the system was warmed up once more at the low setting and once its temperature plateaued the lights were switched to high. The focus was to see how much warmer the hot light setting can make the camera compared to the low setting. Results of this process are presented in **Section 4.1**.

3.3 Reflectance Standards

To calibrate the NIR HSI system, Spectralon Diffuse Reflectance Standards were selected from Labsphere. These standards were durable, range from 2 to 99% and were spectrally flat across the UV-VIS-NIR electromagnetic spectrum. The specific standards selected were URSS-04-010 and include nominal reflectance factors of 2, 50, 75 and 99% (for the remainder of this thesis the standards are referred to using their nominal reflectance values). The dimensions of each standard are 38.1 mm in diameter and 12.7 mm in

height, with a reflective area of 31.8 mm in diameter. It was noteworthy that the nominal reported reflectance values were not precise because the reflectance values change at different wavelengths. In order to use the reflective standards to calibrate at each wavelength, the true reflectance values must be determined.

The options for Spectralon reflectance standards range from 2 to 99% depending on the set selected and the percentages were calculated based on how well the standard reflects the radiation. The true reflectance values for each standard were verified based on the guidelines from the National Institute of Standards and Technology (NIST). An 8°/hemispherical apparatus measured the true reflectance values of each standard and the results were represented in a graph from wavelengths 250- 2500 nm (**Appendix H**).

3.4 Calibration

Calibration of the NIR HSI system first required turning on the components of the system, starting the computer and allowing the system to stabilize. Using the results of **Section 4.1** it was decided that stabilization required 60 minutes. Next the lens was rotated counterclockwise until the image seen on the computer was blurry. This was accomplished by placing a wooden target, with a height equal to the reflectance standards, under the view of the camera. The image was deemed unfocused when the bull's-eye image was no longer recognizable. Both the halogen incandescent bulbs were replaced, which means they were operating under optimal conditions. As mentioned earlier, there were four reflectance standards available, but to properly calibrate the machine more standards were required. The solution was to employ an optical chopper (model No. MC2000, Thorlabs, Newton, NJ) because selecting the 10 slot chopping blade reduced the amount of light passing through the blade by half as it spun. Placing

the chopper between a standard and the LCTF allowed for the detection of half the amount of reflected light and therefore provided nominal reflectance of 1%, 25%, 37.5% and 49.5% better filling the gap between 2% and 50% nominal standards.

The calibration consisted of imaging the reflectance standards, the reflectance standards mechanically reduced by 50% and the dark current as a data cube in a random order. The dark current data cube was created by placing a piece of black cardboard up against the LCTF for the full 3.5 minutes and thereby filling a data cube with the dark current. The full value standards were scanned the usual way, while the half scans were obtained by placing the standards below the LCTF with the chopper mounted on a brace (**Appendix B**). The chopper was suspended right below the LCTF and blocked almost the entire standard. When everything was set up the optical chopper was turned on at 1000 Hz and data was acquired. The process of imaging each option was repeated three more times with a different sequence.

The data cubes were loaded into Matlab and the spatial dimensions of the cubes were reduced from 640×477 to 200×200 to focus on the area of interest. Each cube of the same reflectance value was organized together as 4D matrices and then all the matrices were organized as a 5D matrix going from lowest reflectance to highest reflectance (i.e. dark current to 99% reflectance). The true reflectance values are obtained from the calibration graph from Labsphere and placed into a matrix cube the same size as the large data cube. The calibration equation used was quadratic (Geladi et al., 2004; Burger & Geladi, 2005) and was determined by running a Matlab function called regstats. The function allowed for the specification of the calibration model (i.e. quadratic) and outputs a number of statistics (i.e. estimated y (here after referred to as $\hat{y}$), adjusted R^2,

mean squared error and betas). $\hat{y}$ are the predicted values and the residuals can be calculated by subtracting the $\hat{y}$ from the known values *y* (Wilcox, 2012). The adjusted R^2 was the adjusted coefficient of determination and explains from 0 to 1 how well the data fits the created line. The larger the number means there was a higher correlation in the variance between the expected and predicted lines (Salkind, 2008). Mean squared error (MSE) was another way to examine the error between the predicted and expected calibration lines. The betas (i.e. $\propto_{ijk}, \beta_{ijk}, \& \gamma_{ijk}$) were the coefficients of regression, which were used as the coefficients in the quadratic equation. Each pixel in the data cube was treated individually as the *x* of the quadratic equation and resulted in the calculation of the predicted new value.

3.5 Outlier Determination

Upon completing the calibration, a mask was applied to the data cube to take into account the outlier pixels and frequencies. The outlier frequencies were determined and removed based on plots displaying the variation at each wavelength, as well as based on previous experiences of what was an outlier frequency. To create a mask for the pixels, the first step was to determine what constitutes an outlier. The residuals of the $\hat{y}$ were calculated by subtracting the true reflectance cube from the $\hat{y}$. The residuals were searched for outliers by using the MAD-Median rule:

$$\frac{|X_i - M|}{\frac{MAD}{0.6745}} > K \qquad (3.1)$$

where X_i was the $\hat{y}$ at a frequency, M was the median value of the $\hat{y}$ at a frequency, MAD was the mean absolute deviation of the $\hat{y}$ at a frequency and K distinguishes whether a value was an outlier or not (Wilcox, 2012). A pixel was an outlier if its value was greater

than the K value of 2.24 or had a value of not a number (NaN). The number of outliers in each dimension was the result of summing the outliers per frequency, per pixel and per regression. It was expected that the outliers per regression were a hypergeometric distribution and not a binomial distribution. The difference being that binomial distributions are the probability of x events (e.g. outliers) occurring in n draws with replacements after every draw, while hypergeometric distributions are the probability of k events (e.g. outliers) occurring in n draws without replacement. The probabilities associated with hypergeometric distributions are expressed in the following equation:

$$p(x) = \frac{\binom{K}{x}\binom{N-K}{n-x}}{\binom{N}{n}} \tag{3.2}$$

where p(x) was the probability of having exactly x outliers in a regression, K was the total outliers in the population, x was the number of outliers in a regression, N was the population size and n was the number of draws. A Matlab function called hygepdf performed the hypergeometric distribution and calculated the expected number of outliers per regression. It can be seen in **Figure 3.3** that the expected number of outliers did not match what was observed.

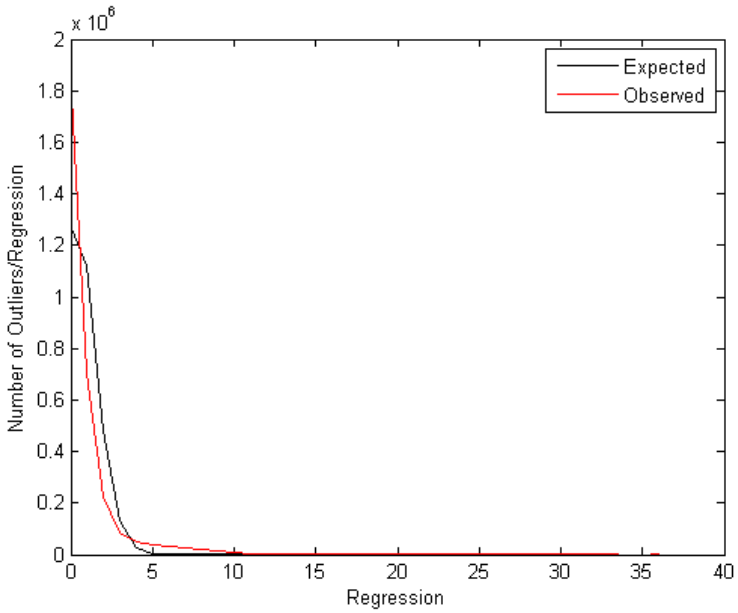

Figure 3.3 Number of outliers/regression

In addition, the expected number was compared to the observed number of outliers per regression by means of a chi squared test. The test resulted in a chi square value of 4.3171e55 and a p-value of 0. This means the null hypothesis was rejected (i.e. the outliers are hypergeometric) and therefore the outliers were not random (Duda et al. 2001). This confirmation justified masking the outliers that occur in the regressions. A bar plot was created to display that the outliers per regression were not hypergeometric, as well as to show a cutoff for outliers. The cutoff separates the acceptable outliers from the true outliers and was identified by the substantial drop in the bars from 359 to 51 outliers per regression (**Figure 3.4**).

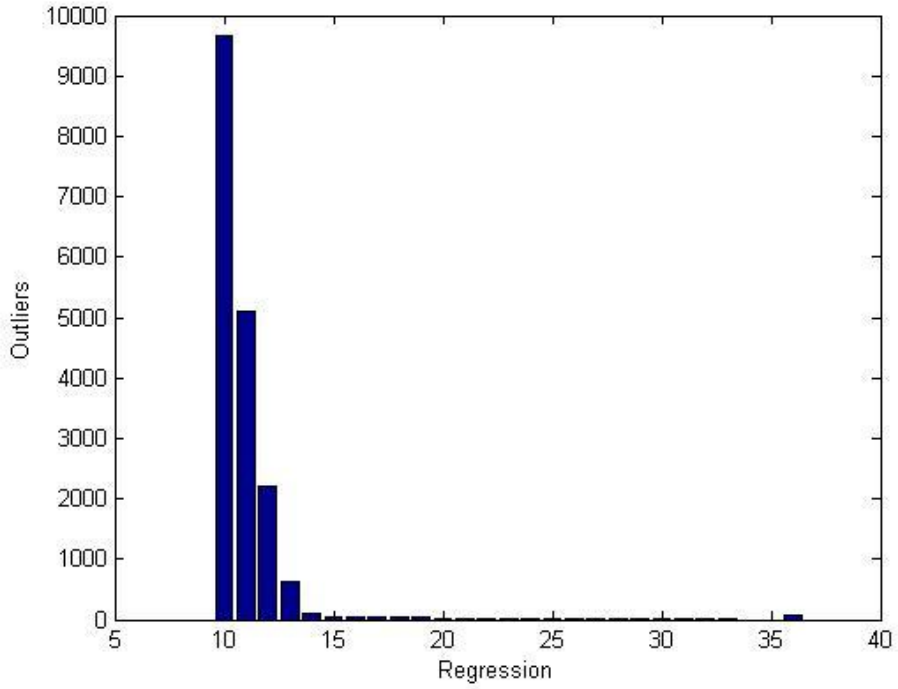

Figure 3.4 Outliers per regression

If the number of outliers per regression was greater than the cutoff, the regression was designated with the value of one in a matrix full of zeros. This allows for the identification of which regressions required masking.

The mask process consists of taking a sample data cube and replacing each outlier location in the cube with the median value at its specific frequency. This reduced the impact each outlier had on its neighbour. Each pixel and its' neighbours are averaged together and used to replace the original value. The locations of the outliers determined earlier were used to index this new cube and the values were placed into the original data cube at the outlier locations. The end result is a data cube with 2,619,188 fewer outliers. After the calibration and masking code were completed, the data acquisition began.

3.6 Data Samples and Data Acquisition

The wheat samples were collected from numerous grain elevator locations across the Canadian prairies and provided for this thesis by Cargill Limited. The samples were from the black soil zone of Manitoba and Saskatchewan and stored inside a freezer at zero degrees Celsius. The sample documentation was recorded into excel based on soil zone, station, grade, Fusarium damage percentage, vomitoxin percentage, protein, moisture content and general comments. After examining the samples it was decided that two bags per grain grade, each sampled twice, would suffice for the samples.

The data acquisition was broken up into three parts: density determination, wheat kernel imaging by NIR HSI and moisture content determination. A multivolume pycnometer (Model No. 1350, Micromeritics, Norcross, GA) was used to determine the unknown density of a sample. The pycnometer works by filling up a specific cup with a sample and measuring the changes in gas pressure as helium is added and removed. The volume of the sample can be determined by solving the following equation:

$$V_{samp} = V_{cell} - \left(\frac{V_{exp}}{\left(\frac{P_1}{P_2}\right) - 1} \right) \tag{3.3}$$

where V_{samp} is the sample volume, V_{cell} is the empty volume of the sample cell with the empty sample cup in the place, V_{exp} is the expansion volume, P_1 is the charge pressure and P_2 is the pressure after expansion. The density can be calculated by the following equation:

$$\rho_{samp} = \frac{W_{samp}}{V_{samp}} = \frac{Gross\ Weight - Cup\ Weight}{V_{samp}} \qquad (3.4)$$

where ρ_{samp} is the density of the sample and W_{samp} is the sample weight. The density determination procedure began by performing the initial calibration of the pycnometer. Calibration consists of recording the P_1 and P_2 for all three of the sample cup sizes each of which is initially empty and then filled with a metal ball of known mass. Simple calculations result in the determination of V_{cell} and V_{exp}, which are required for the sample volume calculation (**Equation 3.3**).

After calibration a bag was selected at random for a desired grain grade, and then the contents were poured into a plastic bin and shaken by hand. The 150 cm^3 sampling cup was filled with 50g of kernels and the contents were stored in a freezer within a plastic bag. Each bag was selected at random and allowed to warm at room temperature 20 minutes before use. The temperature of grain is important in density calculations as cold grain occupies a smaller volume than the grain at room temperature resulting in a higher density value. The grain was placed into the pycnometer, where the air that entered with the kernels was purged and replaced with the working helium gas. Three replications of P_1 and P_2 were measured and averaged. The sample was weighed on a digital scale and returned to the freezer. This process was repeated for the second sampling of a bag and for each grain grade. The end result was a total of 16 samples. In addition, to confirm that the pycnometer results were consistent and reliable a second replication was performed (see **Appendix E**). Upon completing the density determination, the samples remained in the freezer to await NIR HSI imaging.

To maintain consistency in the experiments, one fixture/ locating jig was designed and included in the experiment setup. The fixture (**Appendix A**) was designed to fit on top of the NIR imaging area and aligned the imaged petri dish with the LCTFs. Upon setting up the machine, the 99% reference was captured and the lens was refocused with a bulls-eye image. Since the camera has limited area to view a sample, the kernels were arranged on the petri dish with tweezers into a layer that was approximately 1-2 kernels thick. The petri dish was placed on the fixture and the sample was imaged. This process was repeated until all the kernels from the sample bag were imaged. Afterwards the sample was placed back into the freezer and a new sample was selected.

Moisture content of the samples was determined by drying 10g whole kernels at 130°C for 19 h in quadruplicate (ASAE Standards S352.2, APR 1988).The following equation was used to calculate the moisture content:

$$mc_{wb} = \frac{m_{water}}{m_{wet}} * 100 \qquad (3.5)$$

where mc_{wb} was the moisture content as wet basis, m_{water} was the mass of the water evaporated and m_{wet} was the mass of the initial kernels before drying. Once all of the data acquisition was completed, the next step was data analysis. The goal was to examine the data and determine what trends and patterns exist that can help identify Fusarium damage and DON content in the wheat kernel samples.

3.7 Data Analysis

3.7.1 Near-Infrared Hyperspectral Imaging Analysis

The sample data cubes were processed into the correct size of 76×200×200 and then the calculated calibration equation and outlier mask were applied. Afterwards the data cubes pertaining to a sample were stored together into a 4D matrix. The first approach for analysis was to separate the data into testing and training. The samples ranged from 15 to 20 data cubes and to create consistency 15 samples were selected. The cubes for each sample were randomized into four groups (i.e. three groups of four and one group of three). There were four samples for each grade, totaling 16 groups and 60 data cubes, to create a training group of 45 and a testing group of 15. The final training group of 180 was created by organizing samples of all of the grades together, the remaining 60 samples were organized into an additional final testing group. This research originally focused on creating a classifier with the 180 cubes to recognize distinctions between the four grain grades in this research and then test the classifier with the remaining 60 cubes. This approach was not feasible because a regular computer cannot handle the massive size of the data. The alternative second approach was to create 15 groups of 16 data cubes, where the groups contain one data cube from each sample. The data cubes were selected from random groupings of each sample created from the first approach.

To test the validity of the 15 groups, each was used as a training set and applied for the prediction of four random groups testing sets. The model for each group was the result of applying a k-nearest neighbour classifier with k=3 to the training set using Matlab's implementation of a kd-tree. K-nearest neighbour classifier is a prototype classification method, where it consists of training data and class labels. This method

uses a model with m prototypes (training points x_r, r = 1, . . . , m) each from one of the classes. To classify the point x_o, k-nearest neighbour classifier selects the k-closest prototypes in the set of training data within the Euclidean distance to x_o. It classifies by using the majority vote of the k neighbours closest to it and ties are broken at random. K-nearest neighbour classifier is successful in many classification problems because it is simple, powerful and performs well (Friedman, et al., 2008). A random order was created based on the criteria that no group tested against itself, each group tested four different groups and all groups were tested four times (**Table 3.0**).

Table 3.0 Randomized testing order

Group #	Test 1 Group #	Test 2 Group #	Test 3 Group #	Test 4 Group #
1	5	13	8	11
2	14	9	12	7
3	8	7	11	14
4	7	1	15	13
5	13	12	14	1
6	1	14	4	10
7	10	4	6	12
8	9	3	13	2
9	12	15	10	5
10	11	6	2	4
11	15	2	5	9
12	3	11	7	6
13	4	8	3	15
14	6	10	1	3
15	2	5	9	8

The size of the data became an issue based on the length of time to test one group when the training model exceeded a reasonable time duration. To solve this problem a sample of 1000 pixels out of 40000 were chosen at random from each data cube from within that group and used to create a 1-nearest neighbour classifier training model for the group.

Each group was classified by four different classifiers. The results were examined for the cube of spectra that was consistently predicted to be the same grade as the cube they came from. The consistent spectra were then used to create a new model with k=1 and applied to predict the grades for each of the 15 groups. The model classifies grades at a pixel level for each sample in the group. The occurrence of each grade was totaled and used to create percentages of how often the grades occurred per sample in each group. Observing the results of the percentages made it clear that it would be difficult to predict a specific grain grade in a sample.

A different approach was used to identify the existence of either Fusarium or DON in a sample. New labels were created for Fusarium damage and DON content that corresponded to their respective presence in the samples. The labels were filled with zeros and ones, where zero represented no presence and one represented presence. Based on the sample bags, samples 1-4 had negligible levels of Fusarium damage and no DON content, samples 5-8 had Fusarium damage and no DON content and samples 9-16 had both Fusarium damage and DON content. Two models were created from the percentages using a k=3 nearest neighbour classifier, one for Fusarium damage prediction and another for DON content prediction. A cross validation with a k-fold of 5 was performed on each model and used to create predictions for both. A k-fold cross validation divides the data up into k portions (e.g. 5), trains with a portion of the data (e.g. 4/5) and then uses the results to test the remaining data (e.g. 1/5). This process repeats k times with a different portion selected for testing (Friedman, et al., 2008). After each k-fold the predictions were totaled and then a summary table (**Table 3.1**) was created to display the results.

Table 3.1 Configuration of the summary table

	Predicted	**-**	**+**	
Actual	**-**	**TN**	**FP**	**Specificity**
	+	**FN**	**TP**	**Sensitivity**
		Negative Predictive Value	**Precision**	**Accuracy**

The summary table displays how often a data cube was classified as true negatives (TN), true positives (TP), false positives (FP) and false negatives (FN) (Kohavi & Provost, 1998). In the case of testing for Fusarium damage, the true negatives mean how many of the 240 data cubes were correctly classified as having no Fusarium damage, true positives mean how many were correctly classified as having Fusarium damage and false positives and false negatives mean how many were misclassified as one or the other. Also the table displays the sensitivity, specificity, precision, negative predictive value (NPV) and accuracy. The classifications are defined as:

$$Sensitivity = \frac{TP}{TP + FN} \tag{3.6}$$

$$Specificity = \frac{TN}{TN + FP} \tag{3.7}$$

$$Precision = \frac{TP}{TP + FP} \tag{3.8}$$

$$NPV = \frac{TN}{TN + FN} \tag{3.9}$$

$$Accuracy = \frac{TP + TN}{TP + TN + FP + FN} \quad (3.10)$$

These five classifications display how well the predictive classifiers for Fusarium damage and DON content are performing. As well, the classifications provide different ways to interrupt and understand the results seen in **Section 4.3**. Overall, the higher the values seen equates to the better performance of the predictive classifiers.

4 Results and Discussion

4.1 Temperature Distribution

The halogen bulbs performed well at the low light setting and the three positions for the thermocouples displayed similar results. The temperature started at the room temperature of 27ºC and for 49 minutes the temperature continued to rise until it plateaued out at 34ºC (**Figure 4.0**).

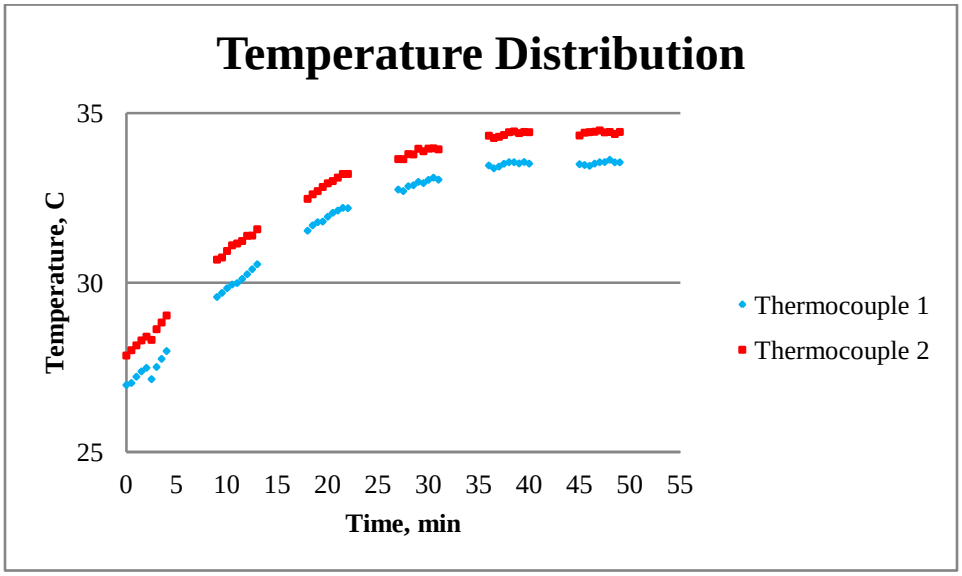

Figure 4.0 Warming up rate with thermocouples at location 1 (low light setting)

At each location, the two thermocouples behaved similarly, with thermocouple one reporting about half a degree warmer than thermocouple two. This may have been caused by a small relative tilt between the two lamps. A further explanation was that the left thermocouple had pulled away from the camera under the tape and although new tape was applied at each location the problem persisted. Furthermore, the time required for the temperature to reach steady state differed between the three locations. Location one took

49 minutes to plateau, location two took 58 minutes and location three took 53 minutes. Results indicated that the first location of the camera reached steady state first, the third and the second required the longest amount of time. This disparity was not deemed to be significant. As well, in all cases there was a period of fluctuation near the end where the temperature climbed by a tenth of a degree every other minute and then dropped by the same amount in between each increase. The temperature was deemed to have reached steady state when the temperature changed by less than a tenth of a degree. It took five minutes of observing the fluctuation for the cut off to be reached.

After the temperature reached a plateau for the first location the lamps are turned off and allowed to cool. The rate of temperature decrease is monitored to gain an understanding of how long the camera requires reaching room temperature again. The temperature started at 4°C below the plateau temperature and decreased by 1.5ºC between ten minute intervals. The starting temperature is different because there is a five-minute gab between when the lamps are turned off and when the data logger starts recording temperatures. After half an hour the temperature fluctuation started and then leveled out (**Figure 4.1**).

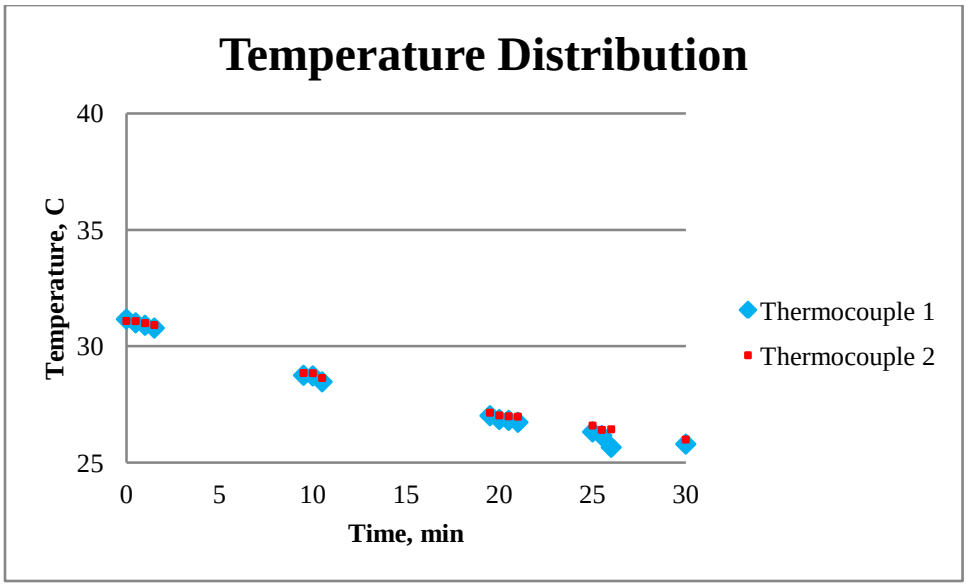

Figure 4.1 Cooling down rate with thermocouples at location 1 (low light setting)

The temperatures recorded by the two thermocouples followed each other very closely. As well, after the third location reached a plateau, the light setting was switched to high to determine how much higher the temperature on the camera can reach. The goal was to see how much the temperature climbed with the new setting (**Figure 4.2**).

The temperature began at the plateau value of the low lamp setting and over the course of 20 minutes increased to a final temperature of 35°C. This was good to know because it was well below the maximum operating temperature of 40°C for the camera. It was decided that the warm up time for the system was 60 minutes. The length of time was based on the fact that the low lamp setting took about an hour, but the high setting produces more heat and therefore heated up fast. In addition, Castorena-Martinez (2009) operated the same NIR HSI system at the 60 minute warm up time with no reported problems.

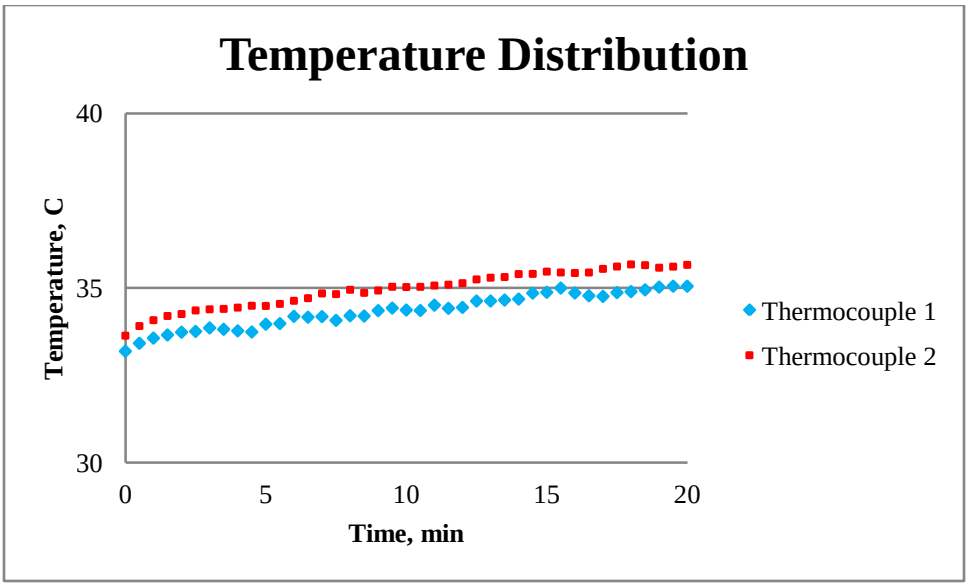

Figure 4.2 Warming up rate with thermocouples at location 3 (high setting)

Likewise, there had been two verbal confirmations that the system requires 30 minutes to warm up. Overall, the 60 minute warm up provided enough time for the system to have a uniform temperature and no irregularities were observed that could influence results.

4.2 Density and Moisture Content

The kernel density of wheat ranges between 1430 and 1449$\frac{kg}{m^3}$ (Grabowski et al. 2012). The measured densities of the samples ranged between 1424 and 1442$\frac{kg}{m^3}$ (**Appendix E**). The measured results fell within the expected range, as well were mildly lower since Fusarium damaged kernels have lower densities (Tkachuk et al., 1991). Examining the two replicates for each grain grade, it can be seen that the pycnometer was consistent with the density measurements. In some instances there were slight differences, but the consistency was evident by looking at the variances and inter quantile range (IQRs). The second sample for each bag displayed similar densities to the first sample with small

variation and IQR. A larger difference was seen between the two bags of each grain grade. The average, variance, median and IQR are calculated in regards to each bag to get a better understanding of how the bags were different and display how it affects the results (**Table 4.0**).

Table 4.0 The average, variance, median and IQR of the measured densities/grade

Grade		Average	Variance	Median	IQR
No. 1 CWRS					
	Samples 1 & 2	1441.54	12.25	1439.88	5.885
	Samples 3 & 4	1438.87	11.77	1439.51	5.304
	All samples	1440.21	13.35	1439.47	5.007
No. 2 CWRS					
	Samples 5 & 6	1437.79	7.179	1437.17	2.383
	Samples 7 & 8	1440.01	14.59	1438.26	5.714
	All samples	1438.90	11.69	1437.94	4.421
No. 3 CWRS					
	Samples 9 & 10	1439.75	13.51	1440.12	3.848
	Samples 11 & 12	1414.30	5.730	1421.37	1.346
	All samples	1427.02	178.1	1425.88	25.66
CW Feed					
	Samples 13 & 14	1440.92	3.712	1440.78	2.605
	Samples 15 & 16	1430.92	7.393	1432.02	3.031
	All samples	1435.92	31.40	1436.84	10.15

The two bags for No. 1 CWRS and No. 2 CWRS were similar to each other with a difference of $3\frac{kg}{m^3}$ for average and an even smaller difference for median. Grade No. 3 CWRS had a difference of $25\frac{kg}{m^3}$ for the average and the median was a difference of $19\frac{kg}{m^3}$. CW Feed had a difference of $10\frac{kg}{m^3}$ for the average and $5\frac{kg}{m^3}$ for the median. It was observed that the density started to decrease with an increase in Fusarium damage, but this cannot be confirmed with the samples measured here given the inconsistencies between the No. 3 CWRS and CW Feed bags. Alternatively, by ignoring grades No. 2 and No. 3 the expected drop in density was observed between the healthy grain of grade No. 1 and the Fusarium damaged grain of CW Feed.

The expected moisture contents were the reported values at the time of harvest and recorded on the original sample bags along with the other information (**Appendix D**). In all cases the expected and measured moisture contents are similar to each other. In most of the samples the measured value was below the expected with the exception of samples 2 and 15. The corresponding samples of a bag had similar moisture contents, which were expected from samples of the same bag. Comparison of the moisture contents shows that most were similar with the exception of sample 9 and 10 with high values. Examining the comparison tables, the small values for variance and IQR confirms that the moisture content procedure was consistent across the replications (**Appendix F**). As seen with density, the moisture content between the bags of each grade showed larger differences. This confirmed that the bags were different from each other. The average, variance, median and IQR are calculated to display the trends (**Table 4.1**).

Table 4.1 The average, variance, median and IQR of the measured moisture contents/grade

Grade		Average	Variance	Median	IQR
No. 1 CWRS					
	Samples 1&2	12.42	0.015	12.42	0.173
	Samples 3&4	13.08	0.026	13.03	0.228
	All samples	12.75	0.133	12.75	0.572
No. 2 CWRS					
	Samples 5&6	12.08	0.014	12.06	0.036
	Samples 7&8	12.16	0.005	12.14	0.034
	All samples	12.12	0.010	12.11	0.108
No. 3 CWRS					
	Samples 9&10	13.89	0.003	13.92	0.095
	Samples 11&12	12.44	0.004	12.46	0.074
	All samples	13.17	0.555	13.16	1.455
CW Feed					
	Samples 13&14	12.50	0.010	12.49	0.162
	Samples 15&16	12.13	0.019	12.10	0.129
	All samples	12.31	0.049	12.38	0.400

Differences between the average and median existed between all bags for each grade. Grade No. 1 CWRS had a difference of 0.6% for both average and median, while No. CW Feed had a similar difference of 0.3% for both. Grade No. 3 CWRS had the largest difference of 1.4% and No. 2 CWRS had the smallest difference of 0.08% for both. In all

cases the average and median were almost the same, which showed that no outliers existed. If there were any outliers, the average would have been different from the median. As with the density, a pattern was difficult to determine with the moisture content. It was expected that with increased Fusarium damage the moisture content would decrease. This was true for No. 1 CWRS and 2 CWRS, but higher moisture content values for 3 CWRS and CW Feed made it difficult to confirm a pattern. The high moisture content of samples 9 and 10 increased the average for grade 3, but the average for CW feed was still higher than 2 CWRS. Disregarding grades 2 and 3, the expected moisture content drop was observed between grade 1 and the feed grain.

The differences observed in the densities and moisture contents can result from different climatic conditions during the time of harvest. It was expected that similar grain grades would have similar densities and moistures, but sample 11 and 12 were harvested from Nicklen Siding, Saskatchewan, while sample 9 and 10 were from Elva, Manitoba. With the exception of sample 11 and 12, the rest of the samples were all from locations in Manitoba. All samples had the same soil zone of black, but a different province might have had different weather and moisture. On the other hand, samples 13, 14, 15 and 16 were all from Elva, MB and there were differences between the bags. Also, the two grades had higher moisture contents than expected to observe a trend. It was expected that wheat kernels with lower density and moisture content would have more Fusarium damage. Another issue was the age of the wheat kernels. The No. 1 CWRS and 2 CWRS were fresher, while No. 3 CWRS and CW Feed were older. That could account for the irregularities observed between grades.

4.3 Near-Infrared Hyperspectral Imaging

Consistent spectra were found by classifying each group with four different classifiers and selecting the spectra that performed the best. It was important to find consistent spectra because it made the classifier more accurate and its predictions consistent. The results of spectral consistency can be seen in **Table 4.2 & Table 4.3**.

Table 4.2 Consistency of spectra

Times Correctly Predicted	Number of Such Spectra	% of Spectra in This Class
0	4684306	48.8
1	3756281	39.1
2	972734	10.1
3	166485	1.8
4	20194	0.2

Table 4.3 Breakdown of grades in the consistent spectra

Grade	Number Consistent from this Grade
1	14027
2	956
3	779
Feed	4432
Total	20194

Results show that the majority of the spectra was either correctly predicted once or not at all. A smaller portion of the spectra was predicted correctly twice or three times. The spectra of interest were the 20194 out of 9,600,000 spectra that were correctly predicted all four times. Examining the consistent spectra in **Table 4.3**, over two thirds were No. 1 CWRS, while the remaining was divided amongst the other three grades. It seems it was

difficult to detect the subtle differences between grades No. 2, No. 3 and feed grade in the spectra. These 20194 spectra were selected for the creation of a prediction model that classified the 15 groups by percentages of grade occurrence. The average of the consistent spectra can be seen in **Figure 4.3**.

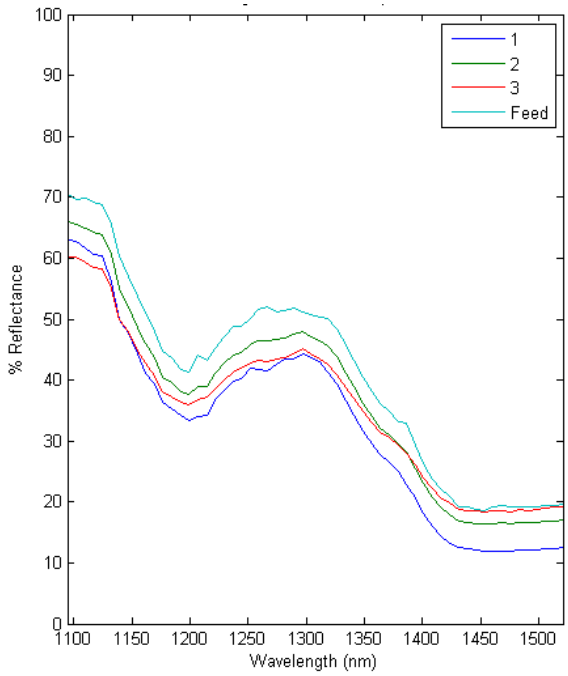

Figure 4.3 Average of consistent spectra

The purpose of creating percentages of grade occurrence per sample in each group was to see if it reflected the expected outcome. Since the samples were organized in order with grades grouped together it was expected that the first four would have a higher percentage for No. 1 CWRS. The next four were No. 2 CWRS and would have a higher percentage for grade two than the others. This expected outcome would continue on for the No. 3 CWRS and CW Feed samples. After examining the percentages for each group it can be seen that the expected trend was not achievable. An example of the percentage

results is displayed in T**able 4.4**, where the predicted grades are tabulated for each sample in group 15.

Table 4.4 Predicted grades of samples in group 15

Sample #	No. 1 CWRS	No. 2 CWRS	No. 3 CWRS	CW Feed
1	0.8104	0.0560	0.0330	0.1006
2	0.8931	0.0469	0.0387	0.0213
3	0.2709	0.1021	0.0326	0.5944
4	0.8289	0.0549	0.0420	0.0743
5	0.1952	0.1160	0.0362	0.6527
6	0.8552	0.0724	0.0454	0.0270
7	0.8247	0.0772	0.0604	0.0377
8	0.2478	0.1424	0.0475	0.5624
9	0.4457	0.0803	0.0695	0.4045
10	0.8689	0.0571	0.0348	0.0392
11	0.1401	0.1315	0.1483	0.5802
12	0.6259	0.0969	0.2390	0.0384
13	0.1203	0.1089	0.0607	0.7102
14	0.1650	0.1025	0.0558	0.6767
15	0.1572	0.1276	0.0539	0.6613
16	0.1624	0.1262	0.0439	0.6676

Samples 1, 2 and 4 had the highest percentages for No. 1 CWRS, which was expected to occur. The exception being sample 3 because it had a higher predicted percentage of CW Feed than No. 1 CWRS. Samples 5-12 displayed an inability to have reliable predictive results. In these samples the prediction was either high for No. 1 CWRS or CW Feed, but never No. 2 or 3 CWRS. Samples 13-16 showed a consistent ability to predict high percentages for CW Feed, which was expected. The same trend was observed in the other 14 groups that the prediction classifier was accurate for distinguishing between No. 1 CWRS and CW Feed, but inaccurate for the other two grades (**Appendix G**). The ability to positively identify one or the other lead to the application of creating a new model

focused on determining the existence of Fusarium damage and DON content in samples. If the model can detect that a sample was CW Feed then that should be a good indication that it can detect the presence of Fusarium damage and/or DON content in the sample.

The creation of two new labels, one for identifying Fusarium damage and the other for identifying DON content, allowed a way to confirm the presence of the fungus or mycotoxin in a sample. After performing the cross validation the results were displayed in summary tables (**Table 4.5 & Table 4.6**).

Table 4.5 Summary table of Fusarium damage

	Predicted	-	+	
Actual	-	39	21	65
	+	14	166	92
		74	89	85

Table 4.6 Summary Table of DON content

	Predicted	-	+	
Actual	-	99	21	83
	+	28	92	77
		78	81	80

It can be seen that of the 240 data cube samples, 53 were classified as negative for Fusarium damage and 187 were classified as positive for Fusarium damage. Breaking it down, 39 were correctly classified as negative for Fusarium damage, 21 were misclassified as positive for Fusarium damage, 14 were misclassified as negative for Fusarium damage, and the remaining 166 were correctly classified as positive for Fusarium damage. As well of the 240 samples, 127 were classified as negative for DON

content and 113 were classified as positive for DON content. Looking at it individually, 99 data cubes were correctly classified as negative for DON content, 21 were misclassified as positive for DON content, 28 were misclassified as negative for DON content and 92 were correctly classified as positive for DON content. In all categories, the prediction classifier for Fusarium damage performed well, with the exception of the 65% specificity. The high accuracy value of 85% demonstrates the model had promise for success. As well, the DON content prediction classifier had similar results as the Fusarium damage model and performed well in all areas with an accuracy of 80%. These results are promising and display potential for future applications.

The final application of these results would be to repeat the sampling procedure on the original samples for another 240 data cube samples. The new samples would be tested with the same prediction classifiers and the results would be compared. The data cubes with a double prediction would be deemed that classification, while the remainder would be manually inspected by an inspector. The five-fold cross validation rates from the prediction classifier would reclassify the data cubes seen in **Table 4.7 & Table 4.8**.

Table 4.7 Reclassification confusion matrix of Fusarium damage

	Predicted	-	+	
Actual	-	74	11	87
	+	26	89	77
		74	89	82

Table 4.8 Reclassification confusion matrix of DON content

	Predicted	-	+	
Actual	-	78	19	80
	+	22	81	79
		78	81	80

The remaining samples without the double confirmation would require individual inspection. The end result would be the ability to acquire two NIR HSI images of wheat kernels in petri dishes and predict the presence of Fusarium damage and DON content by running the analysis code.

5 Conclusions

NIR HSI technology was used to image and create data cubes containing the spectral information about samples of wheat. Wheat samples were organized based on predetermined industry grading standards for wheat and this provided the basis for the sample selection of four grades. The NIR HSI system was monitored with thermocouples to observe the duration of time required to reach the optimal temperature. It was determined that at the highest light setting, the system does not exceed the cameras operating temperature and required 60 minutes to warm up. This initial finding was instrumental because the warm up time was applied to the data acquisition methodology.

Upon acquiring the data cubes, the illuminated region of the focal plane array was isolated by reducing the size of the cubes down from 640×477 to 200×200. This provided the ability to focus on the area of interest and not the areas of dead space or shadows. The NIR HSI system was successfully calibrated by using reflective standards of 2, 50, 75 and 99% and an optical chopper, which provided extra information in the gap of the 2 and 50% standards. The reflectance standards allowed the determination of how the NIR HSI system performed under known values and through regression techniques created a quadratic equation for each pixel in a regression. This calibration provided assurance that the resulting data cubes of the samples would be accurate and reliable.

All the samples selected were measured for density and moisture content. It was expected that a sample with a lower grade would have more Fusarium damage and DON content in it and therefore would have a lower density and moisture content. This would occur because when Fusarium consumes the wheat kernel, the kernel takes on a shrunken

appearance, which would have a lower density and moisture content. The measured values for both density and moisture content showed the potential to exhibit the expected trend, but differences between samples of a given grade made it difficult to determine a trend. More samples would solidify the results and determine if outliers were present in the samples or if it was an expected occurrence.

Through the application of the k-nearest neighbour classifier two classifiers were achieved, where one predicted the existence of Fusarium damage and the other DON content in a given sample of wheat kernels. It was determined that the Fusarium damage prediction classifier had an accuracy of 85%, a sensitivity of 92% and a specificity of 65%, while the DON content prediction classifier had an accuracy of 80%, a sensitivity of 77% and a specificity of 83%. These results establish that the prediction classifiers can be successful in distinguishing if a given sample has Fusarium damage and/or DON content present. Overall, through more research the two prediction classifiers could be introduced into the agriculture industry as a means to identify Fusarium damage and/or DON content in a given wheat sample. The entire manual inspection would not be eliminated, but the classifiers would reduce the time and labor currently being utilized in this process.

6 Recommendations

NIR HSI had success as a detection method for Fusarium damage and/or DON content in a wheat sample. To confirm the reliability of the two classifiers, future work would involve acquiring another set of 240 data cubes from the original samples and applying the prediction classifier. The second prediction on the new data cubes would validate the calculations and results seen in this thesis. As well, the additional new data cubes would provide more data for the analysis on the samples. This would confirm what was observed and solidify the expected trends in moisture content and density.

Along with re-sampling, it would be of interest to acquire a complete new set of samples to determine the existence of similar trends for density, moisture content and prediction classifiers. This thesis displayed the beginnings of a trend and additional data would further help prove the claim that an increase in Fusarium damage and DON content causes a decrease in density and moisture content. As well, differences were observed in density and moisture content values among samples of the same grade. That occurrence was unexpected because samples of the same grade would have similar infection levels and therefore similar density and moisture content levels. More samples would strengthen the results and make it clear whether previously observed values are outliers or general occurrences.

Acquiring images in the visible spectrum after each NIR HSI image would provide further verification and insight into detecting Fusarium damage and/or DON content in wheat samples. The idea would be to use a segmentation technique to group similar characteristics in the image together. Each image would be examined and have k-means

clustering applied to segment the images. The k value equates to the number of groups the image would be broken up into. The correct number of groups is necessary to identify the visible kernels from the background and shadows. Too many or too few groups make the image difficult to interpret. Upon distinguishing between the kernels of interest and the background, the kernels would be examined for the cluster of groups within that image. The interest would be to determine if the groups differentiate between healthy and infected parts of the kernel. The goal would be to apply the segmentation to a sample image and have a result of whether Fusarium damage and/or DON content are present.

Finally, the economics behind applying the prediction classifier as a means for grain inspection would need to be investigated. At the moment, the costs for solely performing manual inspections of grain are unknown. The application of the prediction classifiers would allocate less time towards manual inspection with the technique taking over the majority of the responsibility for identifying the fungus and toxin in grain. This would reduce the amount of time and money required for manual inspection. On the other hand, the cost of misclassifying a sample is unknown. False classification of a sample could result in healthy grain being disposed of or infected grain being consumed. This could cause unnecessary loss to the agriculture industry and requires further research.

7 References

Agriculture and Agri-Food Canada. 2013. Wheat situation and outlook (March 2011). http://www.agr.gc.ca/eng/industry-markets-and-trade/statistics-and-market-information/by-product-sector/crops/crops-market-information-canadian-industry/market-outlook-report/wheat-situation-and-outlook-march-2011/?id=1378845354753. (2014/01/22).

Banwell, C.N. and E.M. McCash. 1994. *Fundamentals of Molecular Spectroscopy*. Berkshire, England: McGRAW-HILL Book Company Europe.

Bauriegal, E, A. Giebel, U. Schmidt and W.B. Herppich. 2011. Early detection of Fusarium infection in wheat using hyper-spectral imaging. *Computer and Electronics in Agriculture*. 75(2): 304-312.

Bennett, J.W. and M. Klich. 2003. Mycotoxins. *Clinical Microbiology Reviews*. 16(3): 497-516.

Blanco, M. and I. Villarroya. 2002. NIR spectroscopy: a rapid-response analytical tool. *Trends in Analytical Chemistry*. 21(4): 240-250.

Booth, C. 1971. *The Genus Fusarium*. Surrey, England: Commonwealth Agricultural Bureaux [for the] Commonwealth Mycological Institute.

Bosco, G.L. 2009. Meeting report- James L. Waters Symposium 2009 on near-infrared spectroscopy. *Trends in Analytical Chemistry*. 29(3): 197-208.

Burger, J. and P. Geladi. 2005. Hyperspectral NIR image regression part I: calibration and correction. *Journal of Chemometrics.* 19: 355-363.

Canadian Grain Commission. 2012. Canadian grain exports: crop year 2011-2012. http://www.grainscanada.gc.ca/statistics-statistiques/cge-ecg/annual/exports-11-12-eng.pdf. (2013/12/17).

Canadian Grain Commission, 2008. Canada Western Red Spring. https://www.grainscanada.gc.ca/wheat-ble/classes/cwrs-eng.htm. (2013/09/04).

Canadian Grain Commission, 2012. Canadian Wheat Classes. https://www.grainscanada.gc.ca/wheat-ble/classes/classes-eng.htm. (2013/09/04).

Canadian Grain Commission. 2013. Wheat- Chapter 4: Official grain grading guide. http://www.grainscanada.gc.ca/oggg-gocg/2013/04-wheat-2013-eng.pdf. (2013/12/17).

Castorena-Martinez, J.E. 2009. Non-uniformity Correction and Calibration of Hyperspectral Image Data. Unpublished M.Sc. thesis. Winnipeg, MB. Department of Biosystems Engineering, University of Manitoba.

Childress, W.L., I.S. Krull and C.M. Selavka. 1990. Determination of deoxynivalenol (DON, Vomitoxin) in wheat by high-performance liquid chromatography with photolysis and electrochemical detection (HPLC-hv-EC). *Journal of Chromatographic Science*. 28: 76-82.

Delwiche, S.R. 2003. Classification of Scab- and Other Mold-Damaged Wheat Kernels by Near-Infrared Reflectance Spectroscopy. *American Society of Association Executives*. 46(3): 731-738.

Delwiche, S.R., M.S. Kim and Y. Dong. 2011. Fusarium damage assessment in wheat kernels by Vis/NIR hyperspectral imaging. *Sensing and Instrumentation for Food Quality and Safety*. 5(2): 63-71.

Dexter, J.E., R.M. Clear and K.R. Preston. 1996. Fusarium head blight: effect on the milling and baking of some canadian wheats. *Cereal Chemistry*. 73(6): 695-701.

Dowell, F.E., M.S. Ram and L.M. Seitz. 1999. Predicting Scab, Vomitotoxin, and Ergosterol in Single Wheat Kernels Using Near-Infrared Spectroscopy. *Cereal Chemistry.* 76(4): 573-576.

Duda, J., P.E. Hart and D.G. Stork. 2001. *Pattern Classification*, 2nd edition. Toronto, Canada. John Wiley & Sons, Inc.

Feng, Y. and D. Sun. 2012. Application of Hyperspectral Imaging in Food Safety Inspection and Control: A Review. *Critical Reviews in Food Science and Nutrition*. 52(11): 1039-1058.

Fischer, C. and I. Kakoulli. 2006. Multispectral and hyperspectral imaging technologies in conservation: research and potential applications. *Reviews in Conservation.* 7: 3-16.

Friedman, J., T., Hastie and R. Tibshirani. 2008. *The Elements of Statistical Learning: Data Mining, Inference and Prediction,* New York, NY: Springer Science + Business Media.

Geladi, P., J. Burger and T. Lestander. 2004. Hyperspectral imaging: calibration problems and solutions. *Chemometrics and Intelligent Laboratory Systems.* 72: 209-217.

Gonzalez, R.C. and R.E. Woods. 2008. *Digital Image Processing*. Upper Saddle River, NJ: Pearson Education Inc.

Goswami, R.S. and H. Corby Kistler. 2004. Heading for disaster: *Fusarium graminearum* on cereal crops. *Molecular Plant Pathology*. 5(6): 515-525.

Grabowski, A., R. Siuda, L. Lenc and S. Grundas. 2012. Evaluation of single-kernel density of scab-damaged winter wheat. *International Agrophysics*. 26: 129-135.

Justice Laws. 2013. Canada Grain Act: R.S.C., 1985, c. G-10. http://laws-lois.justice.gc.ca/eng/acts/G-10/page-1.html#s-2. (2013/12/18).

Kohavi, R. and F. Provost. 1998. Glossary of Terms. *Journal of Machine Learning*. 30: 271-274.

Kos, G., H. Lohninger and R. Krska. 2003. Development of a Method for the Determination of Fusarium Fungi on Corn Using Mid-Infrared Spectroscopy with Attenuated Total Reflection and Chemometrics. *Analytical Chemistry*. 75(5): 1211-1217.

Krska, R., E. Welzig and H. Boudra. 2007. Analysis of fusarium toxins in feed. *Animal Feed Science and Technology*. 137(3): 241-264.

Mortimer, R.G. 1993. *Physical Chemistry*. San Diego, CA: Academic Press.

Osborne, B.G., T. Fearn and P.H. Hindle. 1993. *Practical NIR Spectroscopy with Applications in Food and Beverage Analysis*. Essex, USA: Longman Scientific & Technical.

Ozaki, Y., W.F. McClure and A.A. Christy. 2007. *Near-Infrared Spectroscopy in Food Science and Technology*. New Jersey, NY: John Wiley & Sons, Inc.

Parry, D.W. and P. Nicholson. 1996. Development of a PCR assay to detect Fusarium poae in wheat. *Plant Pathology*. 45(2): 383–391.

Pedrotti, L.S. 2013. Basic Geometrical Optics. In *Fundamentals of Photonics,* ed. C. Roychoudhuri, 1-38. Storrs, CT: SPIE.

Peraica, M., B. Radic, A. Lucic and M. Pavlovic. 1999. Toxic effects of mycotoxins in humans. *Bulletin of the World Health Organization*. 77(9): 754-766.

Pieters, M.N., J. Freijer, BJ. Baars, D. CM Fiolet, J. van Klaveren and W. Slob. 2002. Risk assessment of deoxynivalenol in food: concentration limits, exposure and effects. *Advances in Experimental Medicine and Biology*. 504: 235-248.

Polder, G., G.W.A.M. van der Heijden, C. Wallwijk and I.T. Young. 2004. Detection of Fusarium in single wheat kernels using spectral imaging. *Seed Science and Technology*. 33: 655-668.

Salkind, N.J. 2008. *Statistics for People Who [Think] They Hate Statistics*. Thousand Oaks, USA : Sage Publications, Inc.

Shahin, M.A. and S.J. Symons. 2011. Detection of Fusarium damaged kernels in Canada Western Red Spring wheat using visible/near-infrared hyperspectral imaging and principal component analysis. *Computers and Electronics in Agriculture*. 75(1): 107-112.

Starr, K. 2011. Fourier Transform Infrared Microspectroscopy with Attenuated Total Reflectance as a Detection Method for Fusarium in Whole Wheat Kernels.

Unpublished M.Sc. thesis. Winnipeg, MB. Department of Biosystems Engineering, University of Manitoba.

Statistics Canada. 2013. Field and special crops (production). http://www.statcan.gc.ca/tables-tableaux/sum-som/l01/cst01/prim11b-eng.htm. (2013/12/17).

Tkachuk, R., J.E. Dexter and T.W. Nowicki. 1991. Removal by Specific Gravity Table of Tombstone Kernels and Associated Trichothecenes from Wheat Infected with Fusarium Head Blight. *Cereal Chemistry*.68(4): 428-431.

Wang, W. and J. Paliwal. 2007. Near-infrared spectroscopy and imaging in food quality and safety. *Sensing and Instrumentation for Food Quality and Safety*. 1(4): 193-207.

Windels, C.E. 2000. Economic and social impacts of fusarium head blight: changing farms and rural communities in the northern great plans. *Phytopathology*. 90(1): 17-21.

Wilcox, R.R. 2012. *Introduction to Robust Estimation and Hypothesis Testing*, 2nd edition. San Diego, CA: Elsevier Academic Press.

Appendix A: DESIGN OF NIR HSI FIXTURE

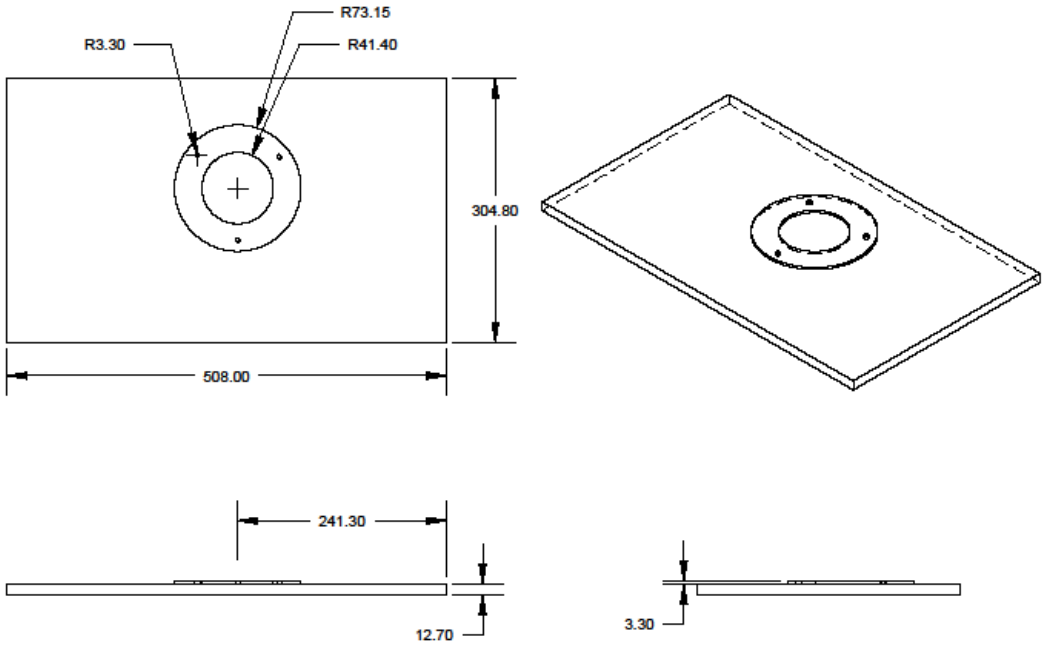

DESIGNED BY JENNIFER BROWN	CHECKED BY N/A	APPROVED BY N/A	DATE 11/16/13	UNITS MILLIMETERS
UNIVERSITY OF MANITOBA		NIR HSI FIXTURE		SHEET 1/1

Appendix B: DESIGN OF CHOPPRER BRACE

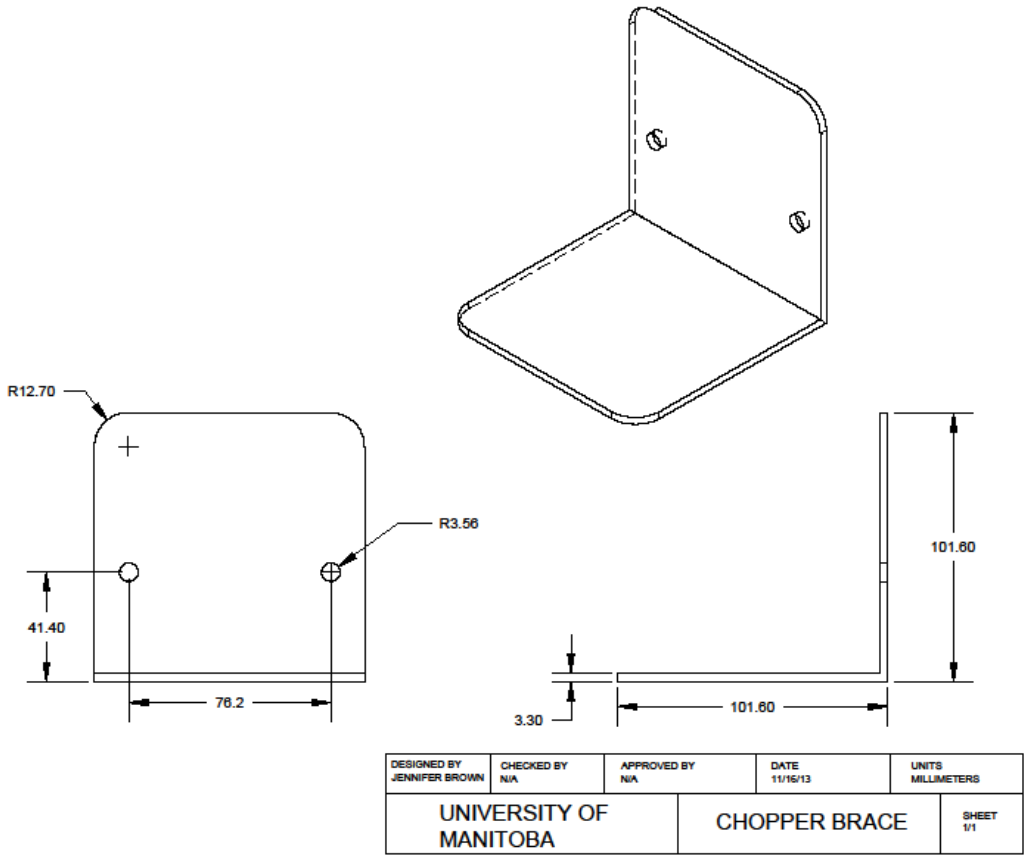

DESIGNED BY JENNIFER BROWN	CHECKED BY N/A	APPROVED BY N/A	DATE 11/16/13	UNITS MILLIMETERS
UNIVERSITY OF MANITOBA	CHOPPER BRACE			SHEET 1/1

Appendix C: CANADIAN GRAIN COMMISSIONS GRAIN GRADING GUIDE - CWRS

Standard of Quality						Foreign material					
Grade name	**Minimum test weight kh/hl (g/0.5 L)**	**Variety**	**Minimum hard vitreous kernels**	**Minimum protein (%)**	**Degree of soundness**	**Ergot (%)**	**Excreta (%)**	**Matter other than cereal grains (%)**	**Sclerotinia (%)**	**Stones (%)**	**Total (%)**
No. 1 CWRS	75 (365)	Any variety of the class CWRS designated as such by order of the Commission	65	10	Reasonably well matured, reasonably free from damaged kernels	0.01	0.01	0.2	0.01	0.03	0.6
No. 2 CWRS	72 (350)	Any variety of the class CWRS designated as such by order of the Commission	No minimum	No minimum	Fairly well matured, maybe moderately bleached or frost-damaged, reasonably free from severely damaged kernels	0.02	0.01	0.3	0.02	0.03	1.2

Standard of Quality						Foreign material					
Grade name	**Minimum test weight kh/hl (g/0.5 L)**	**Variety**	**Minimum hard vitreous kernels**	**Minimum protein (%)**	**Degree of soundness**	**Ergot (%)**	**Excreta (%)**	**Matter other than cereal grains (%)**	**Sclerotinia (%)**	**Stones (%)**	**Total (%)**
No. 3 CWRS	69 (335)	Any variety of the class CWRS designated as such by order of the Commission	No minimum	No minimum	May be frost-damaged, immature or weather-damaged, moderately free from severely damaged kernels	0.04	0.015	0.5	0.04	0.06	2.4
No. 4 CWRS	68 (330)	Any variety of the class CWRS designated as such by order of the Commission	No minimum	No minimum	May be severely frost-damaged, immature or weather-damaged, moderately free from other serevely damaged kernels	0.04	0.015	0.5	0.04	0.06	2.4

Standard of Quality						Foreign material					
Grade name	**Minimum test weight kh/hl (g/0.5 L)**	**Variety**	**Minimum hard vitreous kernels**	**Minimum protein (%)**	**Degree of soundness**	**Ergot (%)**	**Excreta (%)**	**Matter other than cereal grains (%)**	**Sclerotinia (%)**	**Stones (%)**	**Total (%)**
CW Feed	65 (315)	Any class or variety of wheat excluding amber durum and General Purpose	No minimum	No minimum	Reasonably sweet, excluded from other grades of wheat on account of damaged kernels	0.1	0.03	1	0.1	0.1	10
Grade, if specs for CW Feed not met	Wheat, Sample CW Account Light Weight					Wheat, Sample CW Account Ergot	Wheat, Sample CW Account Excreta	Wheat, Sample CW Account Admixture	Wheat, Sample CW Account Admixture	2.5% or less- Wheat, Rejected grade, Account Stones Over 2.5%- Wheat, Sample Salvage	See Mixed grain

Grade name	Contrasting classes (%)	Total (%)	Artificial stain, no residue (%)	Dark Immature (%)	Degermed (%)	Fireburnt	Fusarium damage (%)	Grass green (%)	Grasshopper, army worm (%)	Binburnt severely mildewed rotted, mouldy (%)	Total
No. 1 CWRS	0.75	2.3	Nil	1	4	Nil	0.25	0.75	1	0.005	0.05
No. 2 CWRS	2.3	4.5	0.05	2.5	7	Nil	0.8	2	3	0.02	0.4
No. 3 CWRS	3.8	7.5	0.1	10	13	Nil	1.5	10	8	0.03	1
No. 4 CWRS	3.8	7.5	0.1	10	13	Nil	1.5	10	8	2.5	1

Grade name	Contrasting classes (%)	Total (%)	Artificial stain, no residue (%)	Dark Immature (%)	Degermed (%)	Fireburnt	Fusarium damage (%)	Grass green (%)	Grasshopper, army worm (%)	Binburnt severely mildewed rotted, mouldy (%)	Total
CW Feed	No limit-but not more than 10% amber durum and/or General Purpose	No limit-but not more than 10% amber durum and/or General Purpose	2	No limit	No limit	2	4	No limit	No limit		2.5
Grade, if specs for CW Feed not met	Over 10% amber durum and/or General Purpose-Wheat, Sample CW Account Admixture	Over 10% amber durum and/or General Purpose-Wheat, Sample CW Account Admixture	Wheat, Sample CW Account Stained Kernels			Wheat, Sample CW Account Fireburnt	Wheat, Sample CW Account Fusarium Damage Over 10%-Wheat, Commercial Salvage			Wheat, Sample CW Account Heated	Wheat, Sample CW Account Heated

Grade name	Natural stain (%)	Pink (%)	Sawfly midge (%)	Shrunken (%)	Broken (%)	Total (%)	Smudge (%)	Total (%)	Severely sprouted (%)	Total (%)
No. 1 CWRS	0.5	1.5	2	4	5	7	0.3	10	0.1	0.5
No. 2 CWRS	2	5	5	4	6	8	1	20	0.2	1
No. 3 CWRS	5	10	10	4	7	9	5	35	0.3	3
No. 4 CWRS	5	10	10	4	7	9	5	35	0.5	5
CW Feed	No limit	No limit	No limit	No limit	13	No limit within broken tolerances	No limit	No limit	No limit	No limit
Grade, if specs for CW Feed not met					Sample Broken Grain					

Appendix D: SAMPLE GRADE, LOCATION, SAMPLING NUMBER, PERCENTAGE OF FUSARIUM DAMAGE AND BAG MOISTURE CONTENT

Sample Number	Sample Grade	Sample Location	Bag Number	Sampling Number	Fusarium Damage (%)	Vomitoxin (%)	Bag Moisture Content (%)
1	No. 1 CWRS	Nesbitt	87629	1st	0.256	0	12.5
2	No. 1 CWRS	Nesbitt	87629	2nd	0.256	0	12.5
3	No. 1 CWRS	Elm Creek	87869	1st	0.208	0	13.5
4	No. 1 CWRS	Elm Creek	87869	2nd	0.208	0	13.5
5	No. 2 RS	Oakner	86223	1st	0.6	0	12.3
6	No. 2 RS	Oakner	86223	2nd	0.6	0	12.3
7	No. 2 RS	Oakner	86224	1st	0.35	0	12.4
8	No. 2 RS	Oakner	86224	2nd	0.35	0	12.4
9	No. 3 CWRS	Elva	59508	1st	1.1	1.72	15.2
10	No. 3 CWRS	Elva	59508	2nd	1.1	1.72	15.2
11	No. 3 CWRS	Nicklen Siding	59288	1st	1.2	1.95	12.5
12	No. 3 CWRS	Nicklen Siding	59288	2nd	1.2	1.95	12.5
13	CW Feed	Elva	59281	1st	2.8	1.9	13.0
14	CW Feed	Elva	59281	2nd	2.8	1.9	13.0
15	CW Feed	Elva	59515	1st	1.6	1.07	12.2
16	CW Feed	Elva	59515	2nd	1.6	1.07	12.2

Appendix E: DENSITY COMPARISON TABLES

No. 1 CWRS

Sample	Test 1a	Test 2a	Test 3a	Test 1b	Test 2b	Test 3b	Average	Variance
1	1438.62	1440.03	1439.15	1437.21	1439.72	1439.41	1439.02	1.022
2	1444.57	1445.90	1437.86	1446.44	1443.22	1446.35	1444.06	10.74
3	1434.75	1433.85	1434.25	1438.41	1441.86	1443.71	1437.81	17.87
4	1437.16	1438.91	1438.68	1443.45	1439.54	1441.86	1439.93	5.313
Average	1438.77	1439.68	1437.49	1441.38	1441.09	1442.83		
Variance	17.49	24.45	4.94	18.69	3.143	8.617		

No. 2 CWRS

Sample	Test 1a	Test 2a	Test 3a	Test 1b	Test 2b	Test 3b	Average	Variance
5	1434.58	1438.33	1434.91	1439.84	1437.36	1441.16	1437.70	6.920
6	1443.61	1436.78	1434.96	1436.97	1438.06	1436.99	1437.89	8.851
7	1436.82	1438.49	1436.86	1446.68	1444.50	1442.73	1441.02	17.68
8	1437.83	1433.94	1437.45	1443.87	1439.31	1441.60	1439.00	11.98
Average	1438.21	1436.88	1436.04	1441.84	1439.81	1440.62		
Variance	14.79	4.442	1.709	18.42	10.45	6.304		

No. 3 CWRS

Sample	Test 1a	Test 2a	Test 3a	Test 1b	Test 2b	Test 3b	Average	Variance
9	1433.23	1435.93	1437.41	1440.57	1438.15	1441.17	1437.74	8.741
10	1440.30	1441.45	1437.33	1445.51	1445.95	1439.94	1441.75	11.36
11	1413.93	1414.12	1411.74	1415.55	1416.76	1414.48	1414.43	2.852
12	1415.16	1414.12	1418.54	1413.86	1414.45	1408.85	1414.16	9.710
Average	1425.65	1426.41	1426.26	1428.87	1428.83	1426.11		
Variance	173.1	206.3	172.5	272.2	244.2	283.8		

CW Feed

Sample	Test 1a	Test 2a	Test 3a	Test 1b	Test 2b	Test 3b	Average	Variance
13	1443.04	1442.29	1440.65	1440.91	1441.13	1442.11	1441.69	0.872
14	1439.39	1437.34	1439.55	1444.64	1439.54	1440.49	1440.16	5.891
15	1431.47	1430.76	1431.42	1436.34	1433.37	1434.87	1433.04	4.930
16	1429.99	1429.31	1429.09	1427.93	1428.18	1428.36	1428.81	0.617
Average	1435.97	1434.93	1435.18	1437.46	1435.56	1436.46		
Variance	39.26	36.29	33.40	51.86	35.39	38.76		

No. 1 CWRS

Sample	Test 1a	Test 2a	Test 3a	Test 1b	Test 2b	Test 3b	Median	IQR
1	1438.62	1440.04	1439.15	1437.21	1439.72	1439.41	1439.28	0.890
2	1444.57	1445.90	1437.86	1446.44	1443.22	1446.35	1445.24	2.678
3	1434.75	1433.85	1434.25	1438.41	1441.86	1443.71	1436.58	6.626
4	1437.16	1438.91	1438.68	1443.45	1439.54	1441.86	1439.23	2.537
Median	1437.89	1439.47	1438.27	1440.93	1440.79	1442.784		
IQR	3.553	3.854	1.842	6.089	2.529	3.130		

No. 2 CWRS

Sample	Test 1a	Test 2a	Test 3a	Test 1b	Test 2b	Test 3b	Median	IQR
5	1434.58	1438.33	1434.91	1439.84	1437.36	1441.16	1437.84	3.943
6	1443.61	1436.78	1434.95	1436.97	1438.06	1436.99	1436.98	0.970
7	1436.82	1438.49	1436.86	1446.68	1444.50	1442.73	1440.61	6.793
8	1437.83	1433.94	1437.45	1443.87	1439.31	1441.60	1438.57	3.481
Median	1437.32	1437.55	1435.91	1441.86	1438.69	1441.38		
IQR	3.009	2.299	2.065	5.448	2.722	1.763		

No. 3 CWRS

Sample	Test 1a	Test 2a	Test 3a	Test 1b	Test 2b	Test 3b	Median	IQR
9	1433.23	1435.93	1437.41	1440.57	1438.15	1441.17	1437.78	3.662
10	1440.29	1441.45	1437.33	1445.51	1445.95	1439.94	1440.87	4.465
11	1413.93	1414.12	1411.74	1415.55	1416.76	1414.48	1414.30	1.306
12	1415.16	1414.12	1418.54	1413.86	1414.45	1408.85	1414.28	1.054
Median	1424.19	1425.03	1427.94	1428.06	1427.46	1427.21		
IQR	20.143	23.187	20.514	26.677	23.913	27.177		

CW Feed

Sample	Test 1a	Test 2a	Test 3a	Test 1b	Test 2b	Test 3b	Median	IQR
13	1443.04	1442.29	1440.65	1440.91	1441.13	1442.11	1441.62	1.275
14	1439.39	1437.34	1439.55	1444.64	1439.54	1440.49	1439.55	0.829
15	1431.47	1430.76	1431.42	1436.34	1433.37	1434.87	1432.42	3.060
16	1429.99	1429.31	1429.09	1427.93	1428.18	1428.36	1428.73	1.028
Median	1435.43	1434.05	1435.49	1438.63	1436.46	1437.68		
IQR	9.205	8.181	8.987	7.603	7.869	7.655		

Appendix F: MOISTURE CONTENT COMPARISON TABLES

No. 1 CWRS

Sample	Test 1	Test 2	Test 3	Test 4	Test 5	Average	Variance
1	12.33	12.37	12.38	12.26	12.23	12.31	0.005
2	12.51	12.59	12.53	12.52	12.46	12.52	0.002
3	12.95	12.99	12.91	12.95	12.93	12.94	0.001
4	13.35	13.30	13.19	13.12	13.08	13.21	0.013
Average	12.79	12.81	12.75	12.71	12.67		
Variance	0.206	0.171	0.136	0.156	0.158		

No. 2 CWRS

Sample	Test 1	Test 2	Test 3	Test 4	Test 5	Average	Variance
5	12.24	12.32	12.08	12.06	12.06	12.15	0.015
6	12.06	12.05	12.03	12.00	11.91	12.01	0.004
7	12.31	12.20	12.23	12.14	12.10	12.20	0.006
8	12.13	12.12	12.14	12.16	12.09	12.13	0.001
Average	12.19	12.17	12.12	12.09	12.04		
Variance	0.013	0.014	0.008	0.005	0.008		

No. 3 CWRS

Sample	Test 1	Test 2	Test 3	Test 4	Test 5	Average	Variance
9	13.95	13.92	13.88	13.82	13.79	13.87	0.004
10	13.94	13.94	13.93	13.92	13.83	13.91	0.002
11	12.52	12.52	12.41	12.44	12.35	12.45	0.005
12	12.47	12.49	12.42	12.47	12.34	12.44	0.004
Average	13.22	13.22	13.16	13.16	13.08		
Variance	0.700	0.677	0.740	0.668	0.714		

CW Feed

Sample	Test 1	Test 2	Test 3	Test 4	Test 5	Average	Variance
13	12.41	12.42	12.39	12.38	12.41	12.40	0.000
14	12.61	12.63	12.57	12.57	12.56	12.59	0.001
15	12.48	12.19	12.20	12.13	12.07	12.21	0.025
16	12.09	12.04	12.10	12.01	12.02	12.05	0.002
Average	12.40	12.32	12.31	12.27	12.27		
Variance	0.048	0.068	0.043	0.064	0.070		

No. 1 CWRS

Sample	Test 1	Test 2	Test 3	Test 4	Test 5	Median	IQR
1	12.33	12.37	12.38	12.26	12.23	12.33	0.114
2	12.51	12.59	12.53	12.52	12.46	12.52	0.012
3	12.95	12.99	12.91	12.95	12.93	12.95	0.023
4	13.35	13.30	13.19	13.12	13.08	13.19	0.179
Median	12.73	12.79	12.72	12.73	12.69		
IQR	0.577	0.530	0.488	0.539	0.564		

No. 2 CWRS

Sample	Test 1	Test 2	Test 3	Test 4	Test 5	Median	IQR
5	12.24	12.32	12.08	12.06	12.06	12.08	0.183
6	12.06	12.05	12.03	12.00	11.91	12.03	0.047
7	12.31	12.20	12.23	12.14	12.10	12.21	0.091
8	12.13	12.12	12.14	12.16	12.09	12.13	0.027
Median	12.19	12.16	12.11	12.10	12.08		
IQR	0.149	0.135	0.099	0.099	0.070		

No. 3 CWRS

Sample	Test 1	Test 2	Test 3	Test 4	Test 5	Median	IQR
9	13.95	13.92	13.88	13.82	13.79	13.88	0.099
10	13.94	13.94	13.93	13.92	13.83	13.93	0.025
11	12.52	12.52	12.41	12.44	12.35	12.44	0.106
12	12.47	12.49	12.42	12.47	12.34	12.47	0.055
Median	13.23	13.22	13.15	13.15	13.07		
IQR	1.437	1.412	1.475	1.383	1.449		

CW Feed	Sample	Test 1	Test 2	Test 3	Test 4	Test 5	Median	IQR
	13	12.41	12.42	12.39	12.38	12.41	12.41	0.025
	14	12.61	12.63	12.57	12.57	12.56	12.58	0.040
	15	12.48	12.19	12.20	12.13	12.07	12.19	0.067
	16	12.09	12.04	12.10	12.01	12.02	12.04	0.070
	Median	12.44	12.30	12.29	12.25	12.24		
	IQR	0.179	0.319	0.260	0.328	0.395		

Appendix G: PERCENTAGES OF GRADES PER GROUP (1-14)

Predicted grades of samples in group 1 (left) & group 2 (right)

Sample #	No. 1 CWRS	No. 2 CWRS	No. 3 CWRS	CW Feed
1	0.8865	0.0546	0.0402	0.0187
2	0.8785	0.0494	0.0456	0.0265
3	0.2796	0.0935	0.0447	0.5823
4	0.8829	0.0491	0.0487	0.0193
5	0.2322	0.1426	0.0552	0.5701
6	0.8356	0.0960	0.0416	0.0268
7	0.7163	0.0993	0.0783	0.1060
8	0.2066	0.1664	0.0417	0.5853
9	0.4183	0.0851	0.0549	0.4417
10	0.8419	0.0572	0.0540	0.0469
11	0.2001	0.1322	0.1042	0.5635
12	0.5297	0.0958	0.2511	0.1234
13	0.1338	0.0894	0.0336	0.7432
14	0.1685	0.0907	0.0223	0.7185
15	0.1464	0.0949	0.0524	0.7063
16	0.1902	0.0985	0.0496	0.6617

Sample #	No. 1 CWRS	No. 2 CWRS	No. 3 CWRS	CW Feed
1	0.8836	0.0511	0.0455	0.0198
2	0.8627	0.0540	0.0404	0.0429
3	0.2696	0.1232	0.0390	0.5682
4	0.8752	0.0521	0.0470	0.0258
5	0.1976	0.1007	0.0291	0.6726
6	0.8632	0.0611	0.0543	0.0214
7	0.7927	0.0851	0.0689	0.0533
8	0.1837	0.1282	0.0467	0.6414
9	0.3523	0.0983	0.0746	0.4748
10	0.8448	0.0584	0.0402	0.0567
11	0.1740	0.1221	0.1113	0.5927
12	0.6702	0.0910	0.1678	0.0710
13	0.1655	0.1125	0.0413	0.6808
14	0.1418	0.0937	0.0369	0.7275
15	0.1651	0.1224	0.0356	0.6769
16	0.1777	0.0973	0.0440	0.6810

Predicted grades of samples in group 3 (left) & group 4 (right)

Sample #	No. 1 CWRS	No. 2 CWRS	No. 3 CWRS	CW Feed
1	0.8910	0.0526	0.0323	0.0241
2	0.8652	0.0588	0.0388	0.0372
3	0.2555	0.1209	0.0412	0.5824
4	0.8489	0.0608	0.0556	0.0347
5	0.1956	0.1190	0.0524	0.6330
6	0.8356	0.0671	0.0744	0.0230
7	0.6509	0.1068	0.1253	0.1171
8	0.2063	0.1244	0.0403	0.6290
9	0.2781	0.1305	0.0301	0.5613
10	0.7373	0.0699	0.0657	0.1271
11	0.1365	0.1303	0.1243	0.6089
12	0.6792	0.0827	0.1991	0.0391
13	0.1543	0.1294	0.0371	0.6791
14	0.1665	0.1046	0.0485	0.6804
15	0.2069	0.0961	0.0294	0.6676
16	0.1426	0.1187	0.0657	0.6731

Sample #	No. 1 CWRS	No. 2 CWRS	No. 3 CWRS	CW Feed
1	0.8573	0.0579	0.06123	0.0236
2	0.9130	0.0446	0.0252	0.0173
3	0.2335	0.1094	0.0263	0.6309
4	0.8930	0.0450	0.0391	0.0229
5	0.1441	0.1319	0.0460	0.6780
6	0.6509	0.0903	0.0489	0.2099
7	0.7191	0.0903	0.1257	0.0649
8	0.2243	0.1265	0.0428	0.6064
9	0.3189	0.1098	0.0580	0.5133
10	0.8518	0.0575	0.0583	0.0325
11	0.1509	0.1318	0.1942	0.5232
12	0.5610	0.1023	0.1922	0.1445
13	0.1923	0.0965	0.0394	0.6718
14	0.1991	0.1092	0.0441	0.6477
15	0.1616	0.1261	0.031	0.6813
16	0.1870	0.1170	0.0315	0.6646

Predicted grades of samples in group 5 (left) & group 6 (right)

Sample #	No. 1 CWRS	No. 2 CWRS	No. 3 CWRS	CW Feed
1	0.8459	0.0638	0.0411	0.0493
2	0.8931	0.0473	0.0326	0.0270
3	0.2406	0.1175	0.0335	0.6084
4	0.8373	0.0623	0.0443	0.0562
5	0.1570	0.1289	0.0373	0.6768
6	0.8682	0.0610	0.0430	0.0279
7	0.7263	0.0888	0.0943	0.0907
8	0.1940	0.1320	0.0398	0.6342
9	0.2611	0.1229	0.0416	0.5745
10	0.8541	0.0562	0.0424	0.0474
11	0.1679	0.1232	0.1505	0.5585
12	0.6240	0.0837	0.2343	0.0580
13	0.1343	0.1017	0.0486	0.7155
14	0.2225	0.1053	0.0486	0.6236
15	0.1695	0.1102	0.0364	0.6839
16	0.1698	0.1044	0.0381	0.6877

Sample #	No. 1 CWRS	No. 2 CWRS	No. 3 CWRS	CW Feed
1	0.9221	0.0422	0.0214	0.0143
2	0.8812	0.0475	0.0287	0.0427
3	0.2720	0.0960	0.0290	0.6031
4	0.8851	0.0627	0.0312	0.0210
5	0.1782	0.1184	0.0635	0.6399
6	0.7251	0.0907	0.1161	0.0681
7	0.7885	0.0823	0.0765	0.0528
8	0.1852	0.1352	0.0486	0.6311
9	0.4234	0.0894	0.0654	0.4219
10	0.8450	0.0617	0.0512	0.0422
11	0.1685	0.1270	0.1145	0.5900
12	0.6374	0.0818	0.2331	0.0477
13	0.1838	0.1131	0.0307	0.6724
14	0.1352	0.1102	0.0422	0.7124
15	0.2052	0.0879	0.0365	0.6705
16	0.1740	0.1123	0.0351	0.6786

Predicted grades of samples in group 7 (left) & group 8 (right)

Sample #	No. 1 CWRS	No. 2 CWRS	No. 3 CWRS	CW Feed
1	0.8888	0.0508	0.0376	0.0229
2	0.8573	0.0556	0.0539	0.0334
3	0.3188	0.0887	0.0216	0.5710
4	0.6163	0.0751	0.0402	0.2684
5	0.1923	0.1054	0.0590	0.6433
6	0.7991	0.0801	0.0868	0.0341
7	0.6965	0.1015	0.1383	0.0638
8	0.1998	0.1190	0.0405	0.6407
9	0.2809	0.1088	0.0405	0.5699
10	0.8463	0.0612	0.0503	0.0422
11	0.1539	0.1220	0.1288	0.5953
12	0.7489	0.0770	0.1562	0.0181
13	0.2007	0.1058	0.0570	0.6366
14	0.1656	0.0988	0.0484	0.6873
15	0.1789	0.1143	0.0446	0.6622
16	0.2041	0.1059	0.0371	0.6530

Sample #	No. 1 CWRS	No. 2 CWRS	No. 3 CWRS	CW Feed
1	0.8705	0.0516	0.0331	0.0448
2	0.9024	0.0501	0.0272	0.0203
3	0.2501	0.1109	0.0350	0.6040
4	0.6647	0.0810	0.0488	0.2055
5	0.2107	0.1128	0.0328	0.6438
6	0.8827	0.0630	0.0350	0.0194
7	0.6856	0.1024	0.1360	0.0750
8	0.1736	0.1317	0.0396	0.6552
9	0.4264	0.0919	0.0432	0.4386
10	0.8951	0.0474	0.0359	0.0217
11	0.1368	0.1245	0.1217	0.6171
12	0.6487	0.0898	0.2273	0.0342
13	0.1491	0.1192	0.0486	0.6832
14	0.1907	0.1079	0.0459	0.6555
15	0.1691	0.1154	0.0396	0.6760
16	0.2072	0.1036	0.0571	0.6320

Predicted grades of samples in group 9 (left) & group 10 (right)

Sample #	No. 1 CWRS	No. 2 CWRS	No. 3 CWRS	CW Feed
1	0.6571	0.0720	0.0340	0.2370
2	0.8664	0.0554	0.0419	0.0363
3	0.1843	0.1138	0.0247	0.6773
4	0.8040	0.0679	0.0579	0.0702
5	0.2056	0.1196	0.0340	0.6409
6	0.7760	0.0805	0.0873	0.0563
7	0.7446	0.0802	0.1166	0.0586
8	0.1713	0.1207	0.0369	0.6711
9	0.3067	0.0966	0.0436	0.5532
10	0.8762	0.0652	0.0276	0.0310
11	0.1211	0.1260	0.1324	0.6205
12	0.6284	0.0872	0.2381	0.0463
13	0.1280	0.1200	0.0332	0.7189
14	0.2105	0.0930	0.0234	0.6731
15	0.1535	0.1059	0.0344	0.7063
16	0.1578	0.1209	0.0467	0.6746

Sample #	No. 1 CWRS	No. 2 CWRS	No. 3 CWRS	CW Feed
1	0.8892	0.0504	0.0361	0.0245
2	0.9089	0.0503	0.0248	0.0161
3	0.3213	0.1101	0.0331	0.5355
4	0.8980	0.0481	0.0312	0.0229
5	0.1635	0.1194	0.0549	0.6622
6	0.8706	0.0611	0.0382	0.0302
7	0.7432	0.0893	0.0997	0.0678
8	0.1960	0.1197	0.0320	0.6524
9	0.3639	0.0938	0.0606	0.4818
10	0.8971	0.0528	0.0276	0.0226
11	0.1325	0.1199	0.1185	0.6291
12	0.7041	0.0811	0.1853	0.0295
13	0.1760	0.1005	0.0349	0.6886
14	0.1421	0.1070	0.0340	0.7169
15	0.1477	0.1175	0.0684	0.6664
16	0.2190	0.1224	0.0489	0.6098

Predicted grades of samples in group 11 (left) & group 12 (right)

Sample #	No. 1 CWRS	No. 2 CWRS	No. 3 CWRS	CW Feed
1	0.9297	0.0333	0.0222	0.0148
2	0.9386	0.0299	0.0213	0.0102
3	0.3150	0.1016	0.0216	0.5618
4	0.9121	0.0392	0.0317	0.0170
5	0.1472	0.1693	0.0407	0.6428
6	0.8354	0.1098	0.0348	0.0200
7	0.6990	0.1512	0.0971	0.0527
8	0.2235	0.1818	0.0623	0.5323
9	0.3795	0.0829	0.0628	0.4749
10	0.8801	0.0516	0.0457	0.0218
11	0.1656	0.1299	0.1770	0.5274
12	0.5200	0.0773	0.3185	0.0842
13	0.1261	0.0944	0.0272	0.7523
14	0.1575	0.0946	0.0487	0.6993
15	0.1094	0.1009	0.0435	0.7463
16	0.1287	0.1084	0.0374	0.7255

Sample #	No. 1 CWRS	No. 2 CWRS	No. 3 CWRS	CW Feed
1	0.8795	0.0429	0.0249	0.0527
2	0.9228	0.0393	0.0204	0.0176
3	0.2324	0.1173	0.0550	0.5953
4	0.8622	0.0599	0.0506	0.0274
5	0.1374	0.1170	0.0668	0.6788
6	0.8381	0.0686	0.0593	0.0342
7	0.7812	0.0819	0.1035	0.0334
8	0.2149	0.1237	0.0455	0.6159
9	0.3626	0.1021	0.0777	0.4577
10	0.8841	0.0537	0.0368	0.0253
11	0.1474	0.1129	0.1632	0.5765
12	0.6613	0.0824	0.2093	0.0471
13	0.1420	0.1256	0.0361	0.6963
14	0.1606	0.1029	0.0471	0.6894
15	0.1343	0.1092	0.0854	0.6711
16	0.1705	0.0882	0.0443	0.6971

Predicted grades of samples in group 13 (left) & group 14 (right)

Sample #	No. 1 CWRS	No. 2 CWRS	No. 3 CWRS	CW Feed
1	0.9167	0.0484	0.0209	0.0140
2	0.8887	0.0500	0.0438	0.0176
3	0.2621	0.0868	0.0338	0.6172
4	0.8813	0.0590	0.0336	0.0263
5	0.2269	0.0963	0.0339	0.6429
6	0.7828	0.0725	0.0660	0.0787
7	0.8378	0.0732	0.0584	0.0306
8	0.1952	0.1259	0.0264	0.6525
9	0.4010	0.0925	0.0675	0.4391
10	0.8965	0.0446	0.0375	0.0215
11	0.1945	0.1299	0.1208	0.5549
12	0.7693	0.0716	0.1188	0.0403
13	0.1471	0.1009	0.0306	0.7215
14	0.1616	0.1006	0.0645	0.6733
15	0.1748	0.1090	0.0405	0.6758
16	0.2158	0.1023	0.0389	0.6431

Sample #	No. 1 CWRS	No. 2 CWRS	No. 3 CWRS	CW Feed
1	0.9183	0.0465	0.0198	0.0155
2	0.8934	0.0494	0.0410	0.0162
3	0.2558	0.1056	0.0269	0.6117
4	0.8781	0.0533	0.0393	0.0293
5	0.1792	0.1055	0.0457	0.6696
6	0.8667	0.0716	0.0387	0.0231
7	0.7132	0.0978	0.1077	0.0814
8	0.2287	0.1333	0.0267	0.6113
9	0.3174	0.1177	0.0538	0.5112
10	0.9085	0.0445	0.0292	0.0179
11	0.1508	0.1315	0.1195	0.5983
12	0.6787	0.0861	0.2019	0.0334
13	0.1566	0.1196	0.0501	0.6737
14	0.1822	0.1032	0.0339	0.6808
15	0.1688	0.1349	0.0373	0.6590
16	0.1628	0.1084	0.0368	0.6921

Appendix H: TRUE REFLECTANCE VALUES